Nonlinear shear instabilities of alongshore currents over barred beaches

Donald N. Slinn, J. S. Allen, P. A. Newberger, and R. A. Holman

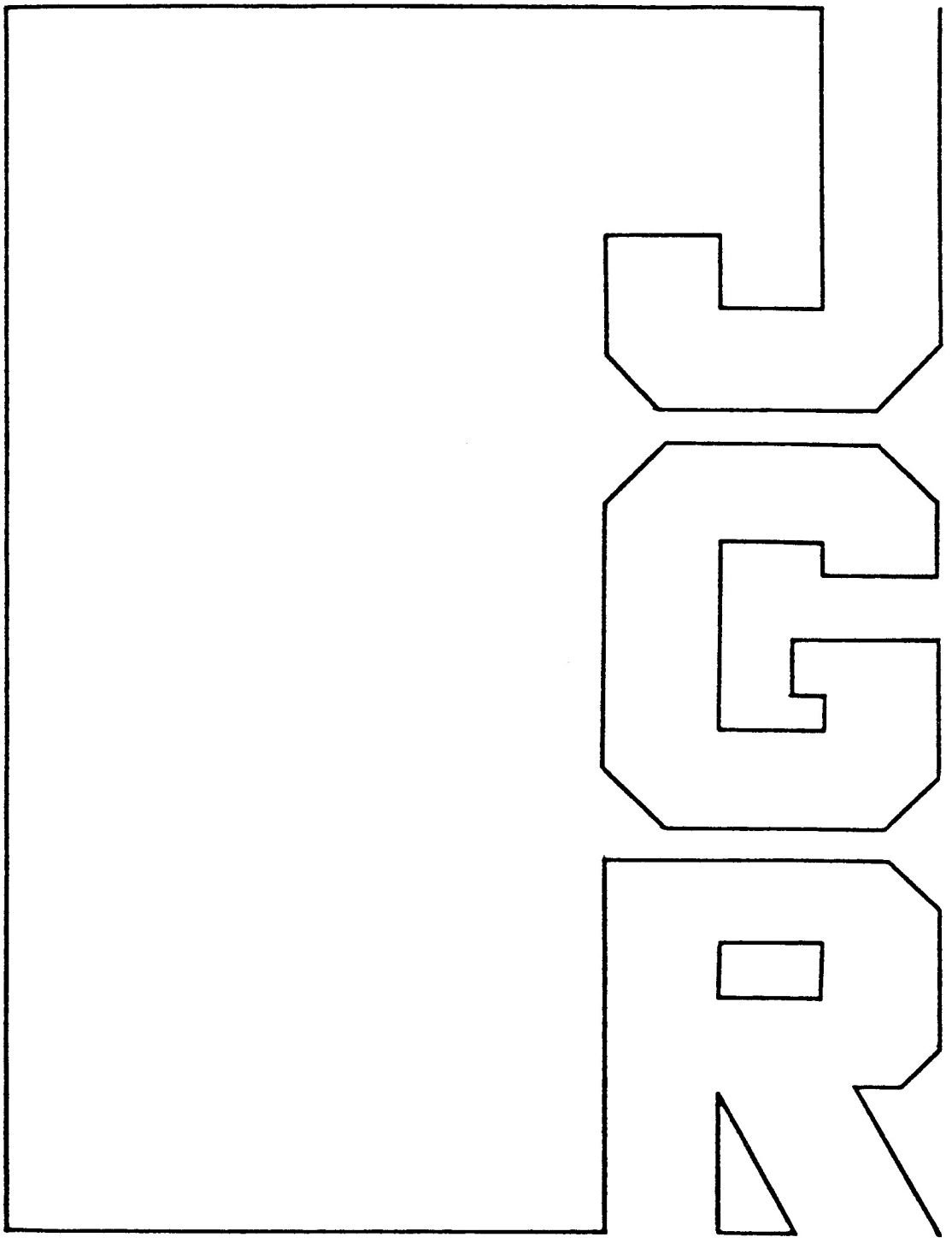

Journal of Geophysical Research. vol. 103. no. C9. Aug. 15. 1998

JOURNAL OF GEOPHYSICAL RESEARCH, VOL. 103, NO. C9, PAGES 18,357–18,379, AUGUST 15, 1998

Nonlinear shear instabilities of alongshore currents over barred beaches

Donald N. Slinn, J. S. Allen, P. A. Newberger, and R. A. Holman

College of Oceanic and Atmospheric Sciences, Oregon State University, Corvallis

Abstract. The nonlinear dynamics of finite amplitude shear instabilities of alongshore currents in the nearshore surf zone over barred beach topography are studied using numerical experiments. These experiments extend the recent study of *Allen et al.* [1996], which utilized plane beach (constant slope) topography by including shore-parallel sandbars. The model involves finite-difference solutions to the nonlinear shallow water equations for forced, dissipative, initial-value problems and employs periodic boundary conditions in the alongshore direction. Effects of dissipation are modeled by linear bottom friction. Forcing for the alongshore currents is specified using a model formulated by *Thornton and Guza* [1986] (T-G). Distinct classes of flows develop depending on the dimensionless parameter Q, the ratio of an advective to a frictional timescale. For Q greater than a critical value Q_C the flows are linearly stable. For $\Delta Q \equiv Q_C - Q > 0$ the flow is unstable. For small values of ΔQ, equilibrated shear waves develop that propagate alongshore at phase speeds and wavelengths that are in agreement with predictions from linear theory for the most unstable mode. At intermediate values of ΔQ, unsteady vortices form and exhibit nonlinear interactions as they propagate alongshore, occasionally merging, pairing, or being shed seaward of the sandbar. At the largest values of ΔQ examined, the resulting flow field resembles a turbulent shear flow. A net effect of the instabilities at large ΔQ is to distribute the time-averaged alongshore momentum from local maxima of the T-G forcing, located over the sandbar and near the shore, into the region of the trough. The across-shore structure of the time-averaged alongshore current is in substantially better qualitative agreement with observations than that given by a steady frictional balance with T-G forcing. The results point to the possible existence in the nearshore surf zone of an energetic eddy field associated with instabilities of the alongshore current.

1. Introduction

Observations in the nearshore surf zone at Duck, North Carolina, by *Oltman-Shay et al.* [1989] showed the existence of alongshore propagating disturbances associated with the presence of alongshore currents. The observed propagating disturbances have different character than surface gravity waves because their wave periods ($\simeq$100 s) are too long in comparison with their wavelength ($\simeq$100 m) to be gravity waves. *Bowen and Holman* [1989] used linear analysis to show that the disturbances could be caused by shear instabilities in the alongshore currents. *Dodd et al.* [1992] obtained good agreement of wavelengths and wave speeds from observations and from theoretical predictions based on the most unstable mode from a linear stability analysis using realistic estimates of mean currents and barred beach bottom topography and including bottom friction effects.

Paper number 98JC01111.
0148-0227/98/98JC-01111$09.00

Several fundamental aspects of the dynamical behavior of finite-amplitude shear waves over beach topography similar to that at Duck, North Carolina, have yet to be explained. Why do the disturbances retain wavelike properties if they are unstable? Is there an equilibration mechanism at finite amplitude that stabilizes the flow? How does the resulting flow depend on beach topography, dissipation processes, and the alongshore current forcing conditions? *Allen et al.* [1996] addressed some of these questions in a study of nonlinear shear waves on plane (i.e., constant slope) beaches. Observations of shear waves, however, have primarily been reported from field experiments at Duck, North Carolina, on a beach that includes a shore-parallel sandbar. The purpose of our present study is to extend the work of *Allen et al.* [1996] to include barred beaches. The primary objective is to examine the effect that the barred beach topography has on the resulting nonlinear flows with forcing specified by the model of *Thornton and Guza* [1986].

With regard to other studies of the finite-amplitude behavior of shear instabilities we note that some prelim-

inary results have been obtained by *Dodd and Thornton* [1993] using weakly nonlinear theory and by *Falques et al.* [1995], *Deigaard et al.* [1995], and *Ozkan-Haller and Kirby* [1997] using numerical experiments.

The numerical experiments of *Allen et al.* [1996] involved finite-difference solutions to the nonlinear shallow water equations for dissipative, initial-value problems with idealized forcing. It was shown that the flow response depends on a dimensionless parameter $Q = \mu L/V_M h_0$, representing the ratio of an advective to a frictional time scale, where μ is the bottom friction coefficient, V_M is the maximum alongshore velocity, and h_0/L is the beach slope. Below a critical value Q_C, the flows are linearly unstable, and disturbances grow initially at the wavelength of the most unstable linear mode. For small values of $\Delta Q = Q_C - Q$ (≥ 0) the waves equilibrate with constant or time-varying amplitudes. For larger values of ΔQ the unstable waves evolve into longer-wavelength, nonlinear, propagating, steady or unsteady, wave-like disturbances.

The barred beach model utilized in the present study is forced by the *Thornton and Guza* [1986] alongshore current model, which is based on a time-averaged momentum balance between the across-shore gradient of the wave-induced momentum flux from obliquely incident, breaking surface waves and the alongshore bed shear stress. The *Thornton and Guza* [1986] (hereinafter referred to as T-G) model has been successful at predicting observed mean alongshore current profiles on plane beaches. The model, however, has not been as successful for barred beaches, where it predicts that the largest currents will be found over the bar and at the coast, with relatively small currents in the trough shoreward of the sandbar [e.g., *Church and Thornton*, 1993]. Strong alongshore currents are often observed in the trough, however, in contrast to the predictions of the T-G model [e.g., *Smith et al.*, 1993]. These discrepancies have led to investigation of other horizontal diffusive processes by which momentum input from obliquely incident breaking waves could be distributed. Other approaches have been to include horizontal turbulent eddy diffusivities [e.g., *Battjes*, 1975; *Thornton and Guza*, 1986] or breaking wave roller models that broaden the region of momentum input [e.g., *Svendsen*, 1984] in the T-G type models. We purposefully use the basic T-G model without modification of the forcing mechanism to assess the effects of horizontal momentum diffusion from current instabilities alone and to avoid complications from the inclusion of additional uncertain horizontal diffusive processes.

Several questions concerning the behavior of alongshore currents when sandbars are present remain unanswered. Can the existence of significant mean alongshore currents in the trough be related to the presence of instabilities in the alongshore current? Does the T-G model make reasonable predictions for the forcing from obliquely incident breaking surface waves, but is the time-mean momentum then redistributed by Reynolds stresses associated with the instabilities? Does the presence of a sandbar change the flow behavior from that observed over plane beaches? We attempt to address these questions by conducting numerical experiments.

Our approach is to select barred beach profiles similar to topography measured at Duck, North Carolina. The topography is held fixed for each set of experiments in which the bottom friction coefficient is varied. The observed flow behavior for barred beaches with T-G forcing is found to have strong qualitative differences from the behavior obtained for plane beaches. To examine and verify the generality of these differences, we present results from experiments with two different barred beach profiles. We emphasize that in these experiments we focus on a study of the dependence of the general characteristics of the flow on the magnitude of Q through variations in the bottom friction coefficient μ and we do not pursue detailed comparisons with field data. The nature of the flow response is found to be sensitively dependent on the value assumed for the bottom friction coefficient. Given this sensitivity and the fact that quantitative representations of bottom frictional processes in the surf zone are not well established, we feel the present process-oriented studies are a desirable prerequisite to studies that attempt direct simulations of conditions during field experiments.

The paper is organized into four sections. Section 2 contains the problem formulation. The numerical experiments are described in section 3. Section 3.1 introduces the basic flow features, section 3.2 contains analysis of integrated flow properties, and section 3.3 presents results related to alongshore propagation rates. A summary and conclusions are given in section 4.

2. Formulation

Numerical experiments involving finite-difference solutions to the shallow water equations for idealized, forced, dissipative, initial-value problems are utilized to study the nonlinear dynamics associated with shear instabilities of alongshore currents in the surf zone over beaches with shore-parallel sandbars. We select the simplest fluid dynamical system that retains the essential physics of this problem. The model geometry is periodic in the alongshore direction and bounded offshore of the region of interest by a vertical wall (Figure 1). Forcing effects from obliquely incident breaking surface waves are approximated by a steady body force in the alongshore momentum equation. Dissipation is modeled by linear bottom friction. Weak biharmonic friction is included to provide additional numerical dissipation at high wavenumbers in the finite-difference solutions. The rigid-lid approximation is also invoked.

The governing shallow water equations are employed in dimensional form as

$$(hu)_x + (hv)_y = 0 \,, \tag{1a}$$

$$u_t + uu_x + vu_y = -\frac{p_x}{\rho_0} - \mu\frac{u}{h} - \nu\nabla^4 u \,, \tag{1b}$$

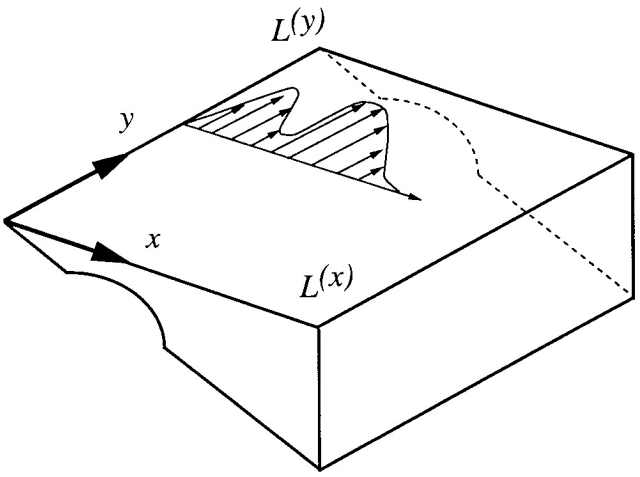

Figure 1. Schematic of the model geometry showing the computational domain. Details of the beach profiles are described in Appendix A.

$$v_t + uv_x + vv_y = -\frac{p_y}{\rho_0} - \mu\frac{v-V}{h} - \nu\nabla^4 v\ , \qquad (1c)$$

where Cartesian coordinates (x, y) are aligned across shore and alongshore, respectively, with $x = 0$ at the coast, t is time, (u, v) are velocity components in the (x, y) directions, p is pressure, ρ_0 is the constant fluid density, $h = h(x)$ is the depth, μ is a bottom friction coefficient, and ν is a small biharmonic diffusion coefficient. A steady forcing term $F = \rho_0\mu V(x, y)/h(x)$ is applied to the y momentum equation to represent momentum input from breaking surface waves.

Dimensionless variables are formed using the characteristic scales (L_S, h_0, V_m) for a horizontal length scale, a depth scale, and a velocity, respectively. The characteristic velocity V_m is related to the magnitude of the forcing based on scaling appropriate for a steady, y independent, forced flow balanced by bottom friction and is chosen as the maximum of the forced profile V_{TGE} (defined below). We choose the horizontal length scale L_S as the across-shore distance from the coast to the x position of the crest of the sandbar where the depth of the water is $h_0 = h(x = L_S)$. The rigid-lid approximation is utilized based on the assumption that the characteristic timescale is the advective timescale $t_C = L_S/V_m$ and on the scaling estimate that $V_m^2 \ll gh_0$, where g is the acceleration of gravity [e.g., *Bowen and Holman*, 1989]. The latter condition is reasonably well satisfied for typical scale values $V_m \approx 1$ m s^{-1} and $h_0 \approx 2$ m. With dimensionless variables denoted by stars we have

$$(x, y) = (x^\star, y^\star)L_S, \qquad (2a)$$

$$t = t^\star L_S/V_m, \qquad (2b)$$

$$h = h^\star h_0, \qquad (2c)$$

$$(u, v) = (u^\star, v^\star)V_m, \qquad (2d)$$

$$p = p^\star \rho_0 V_m^2, \qquad (2e)$$

$$V = V^\star V_m. \qquad (2f)$$

The equations in (1) in dimensionless variables (dropping the stars) are

$$(hu)_x + (hv)_y = 0\ , \qquad (3a)$$

$$u_t + uu_x + vu_y = -p_x - Q\frac{u}{h} - R^{-1}\nabla^4 u\ , \qquad (3b)$$

$$v_t + uv_x + vv_y = -p_y - Q\frac{v-V}{h} - R^{-1}\nabla^4 v\ , \qquad (3c)$$

where

$$Q = \mu\, L_S/(V_m\, h_0)\ , \qquad (4)$$

$$R^{-1} = \nu/(V_m L_S^3)\ . \qquad (5)$$

In general, we consider $R^{-1} \ll 1$ so that Q is the primary dimensionless parameter upon which the solutions depend. Note that Q represents the ratio of an advective timescale L_S/V_m to a frictional timescale h_0/μ. The numerical experiments reported here are performed in dimensional variables. The dynamical similarity for a specified beach bathymetry indicated by the dimensionless equations (3) and the dependence on the dimensionless parameters Q and R^{-1} can be recovered, of course, by rescaling. Henceforth we use (1) and dimensional variables.

The basic geometry of the model is shown in Figure 1. The (x, y) dimensions of the domain are $(L^{(x)}, L^{(y)})$. The model is periodic in the y direction with period $L^{(y)} = 1200$ m or $L^{(y)} = 1280$ m. Experiments with longer alongshore domains $1700 < L^{(y)} < 2560$ m have been conducted and demonstrate that the results obtained here are independent of the choice of $L^{(y)}$. We choose $L^{(x)}$ (= 1000 m) large enough that the behavior of the flow is not influenced by the finite domain size in x. Figure 1 shows a sandbar located offshore (Appendix A) and an alongshore velocity profile characteristic of those predicted by the T-G model (Appendix B).

The numerical model is described in detail by *Allen et al.* [1996]. It is a finite difference model written in conservation form on a staggered (C) grid using Adams-Bashforth time stepping and a direct Poisson solver to obtain the pressure field. The grid spacing is uniform $(\Delta x = \Delta y)$ and set at either 2.0 or 2.5 m and the time step $\Delta t \leq 0.2$ s. The biharmonic friction coefficient $\nu = 1.25$ m^4 s^{-1} for 2.0 m grid resolution or $\nu = 2.5$ m^4 s^{-1} for 2.5 m grid resolution. With $L_S \simeq 100$ m and $V_m \simeq 1$ m s^{-1}, (5) gives $R^{-1} \approx 10^{-6} \ll 1$ so that the biharmonic friction, which adds numerical damping at small length scales ($\simeq$4 m), has little influence on the dynamics of the instabilities of interest here.

The boundary conditions in x correspond to no normal flow at the shore and at the offshore boundary, i.e.,

$$hu = 0 \qquad x = 0, L^{(x)}\ . \qquad (6)$$

The biharmonic diffusion operator requires the additional boundary conditions

$$u_{xx} = v_x = v_{xxx} = 0 \qquad x = 0, L^{(x)}\ . \qquad (7)$$

Two representations for the beach bottom topography $h(x)$ with shore-parallel sandbars are utilized. These are described in Appendix A and shown in Figure 2. Also shown in Figure 2 are velocity profiles derived from the *Thornton and Guza* [1986] model (Appendix B) which represent the effective forcing as described below.

The T-G model predicts steady state frictionally balanced alongshore currents V_{TG} for specified wave field parameters using an approximate steady alongshore momentum balance between the gradient of the radiation stress (or wave-induced momentum flux) and the bottom stress. The submodel parameters are specified in Appendix B. The parameter that distinguishes the resulting velocity profiles is the linear coefficient of bottom friction μ. For these experiments, bottom friction coefficients are examined across a range of μ values appropriate for nearshore environments [e.g., *Dodd*, 1994]. Values of μ used for beach 1 (Figure 2, top) are $\mu = 0.00060$, 0.00087, 0.00116, and 0.00145 m s^{-1}. For beach 2 (Figure 2, bottom), $\mu = 0.00085$, 0.00142, 0.00256, and 0.00369 m s^{-1}. If we consider $\mu = C_f\,|u_{\mathrm{rms}}|$, where u_{rms} is the wave orbital velocity and assume

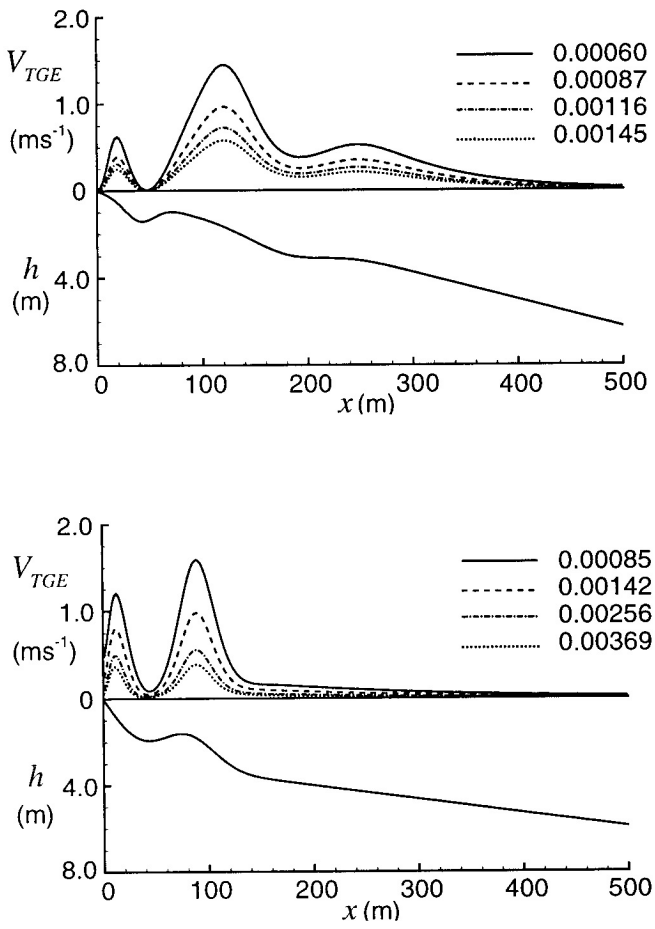

Figure 2. Beach profiles $h(x)$ for (top) beach 1 and for (bottom) beach 2 and velocity profiles $V_{\mathrm{TGE}}(x)$ from the *Thornton and Guza* [1986] submodel for different values of μ (m s^{-1}).

$|u_{\mathrm{rms}}| \simeq 0.3$ m s^{-1} [e.g., *Dodd*, 1994], then the specified values of μ correspond to values of C_f in the range 0.002 – 0.012.

For these experiments we utilize the forcing $V(x,y)$ in (1c) as obtained from the *Thornton and Guza* [1986] submodel with small y dependent perturbations added, i.e.,

$$V(x,y) = V_{\mathrm{TG}}(x)\,[1 + \epsilon b(y)]\ , \tag{8}$$

where

$$\epsilon b(y) = \epsilon \sum_{j=1}^{J} b_j \cos\left(2\pi j y / L^{(y)} - \phi_j\right)\ . \tag{9}$$

For the experiments presented below $\epsilon = 0.001$, $J = 12$, and ϕ_j represent random phases. The sensitivity of the results is examined for different values of ϵ between 10^{-11} and 0.1. It was found that the long time behavior ($t > 5$ h) of the flows is independent of the perturbation amplitude over this range.

The V_{TG} profile for barred beaches results in relatively large gradients and large values near the beach at $x = 0$ as a result of the assumption that all of the shoaling wave energy is dissipated as the wave reaches the shore. This approximation is less realistic for steeper beaches as some wave energy is reflected offshore [e.g., *Elgar et al.*, 1994]. Because of the unrealistically large gradients of V_{TG} between $x = 0$ and 30 m, biharmonic diffusion in (1c) plays a role in this region. Consequently, in order to obtain an expression for the alongshore velocity that would result in a steady balance of T-G forcing with friction, we define $V_{\mathrm{TGE}}(x)$ as the solution to

$$\nu\nabla^4 V_{\mathrm{TGE}} + \mu\frac{(V_{\mathrm{TGE}} - V_{\mathrm{TG}})}{h} = 0\ , \tag{10}$$

with boundary conditions (7), and we regard $V_{\mathrm{TGE}}(x)$ as representing the effective forcing. For $x > 30$ m, biharmonic diffusion plays a minor role in the momentum balance, and there is no noticeable difference between V_{TGE} and V_{TG}.

The velocity profiles V_{TGE} associated with beach 1 (Figure 2, top) have three distinct maxima located at approximately $x = 20$, 125 and 250 m. We will sometimes consider these separate velocity peaks to be distinct alongshore jets. Most of the momentum in the velocity profile on beach 1 is contained in the jet centered at 125 m, which is ~55 m seaward of the bar crest. There is very little forcing of the alongshore velocity in the trough located near $x = 50$ m. The forcing velocity profiles V_{TGE} for beach 2 have two distinct alongshore jets. The inner jet reaches a maximum at $x = 15$ m and decreases to a minimum in the trough at $x = 45$ m. The outer jet has a maximum at $x = 90$ m just outside of the bar crest at $x = 80$ m.

The most dynamically significant difference between the velocity profiles on beaches 1 and 2 is that there is stronger shear (i.e., a narrower jet) in the offshore

jet on beach 2. *Bowen and Holman* [1989] and *Allen et al.* [1996] showed that an increase of the shear offshore of the maximum in the velocity profile can lead to an increase in the growth rates and to a decrease in the length scales of the instabilities that develop in the alongshore currents.

For analysis of the experiments it is useful to define the following variables and averaging operations. The vertical component of vorticity is

$$\zeta = v_x - u_y \ , \tag{11}$$

and the potential vorticity is $q = \zeta/h$. From (1a) a transport stream function may be defined such that

$$hu = -\psi_y \ , \quad hv = \psi_x \ . \tag{12}$$

The alongshore and time averages of a quantity are given by

$$\overline{v} = \frac{1}{L^{(y)}} \int_0^{L^{(y)}} v(x,y,t)\, dy \ , \tag{13}$$

$$\langle v \rangle = \frac{1}{\Delta t} \int_{t_i}^{t_f} v(x,y,t)\, dt \ , \tag{14}$$

where $\Delta t = t_f - t_i$. Variables, such as the alongshore velocity, may be divided into mean (time average, alongshore average, or time and alongshore average) and fluctuating parts, as defined by

$$v(x,y,t) = \langle v \rangle + v'(x,y,t) \ , \tag{15}$$

$$v(x,y,t) = \overline{v} + \tilde{v}(x,y,t) \ , \tag{16}$$

$$v(x,y,t) = \langle \overline{v} \rangle + \hat{v}(x,y,t) \ . \tag{17}$$

For the across-shore velocity u we note that with $h = h(x)$ and periodicity in y, (1a) implies $\overline{u} = 0$. Using (10), the time- and alongshore-averaged y momentum equation (1c) can be written

$$\left\langle \overline{\frac{(huv)_x}{h}} \right\rangle + \left\langle \overline{\mu \frac{(v - V_{\mathrm{TGE}})}{h}} \right\rangle + \left\langle \overline{\nu \nabla^4 (v - V_{\mathrm{TGE}})} \right\rangle = 0 \ , \tag{18}$$

where $\overline{huv} = \overline{h\tilde{u}\tilde{v}}$.

3. Results

3.1. Basic Flow Features

The linear stability of the forced velocity profiles over barred beach topography is determined in the standard manner [e.g., *Drazin and Reid*, 1981]. Solutions of the form

$$\tilde{\psi} = \mathrm{Re}\left\{\phi(x) \exp\left[ik(y - (c_r + ic_i)t)\right]\right\} \tag{19}$$

for the perturbation streamfunction $\tilde{\psi}$ are obtained numerically from the linearized potential vorticity equation as a function of the alongshore wavenumber k. The method of solution, discussed in Appendix C, is similar to that utilized in *Allen et al.* [1996], with the exception that the biharmonic diffusion terms are included here. The real part of the phase speed c_r gives the alongshore rate of propagation of the linear modes, while the imaginary part multiplied by k gives the growth rate kc_i. Positive values of kc_i indicate unstable modes while negative values indicate modes that decay in time.

The growth rate kc_i for the most unstable linear mode is plotted as a function of k for beach 1 in Figure 3 (top) for different values of the bottom friction coefficient μ. The velocity profiles used in the linear stability calculations are the V_{TGE} profiles (Appendix C). Figure 3 shows that all of the velocity profiles are linearly unstable at the specified values of μ with the fastest-growing linear mode for beach 1 having a wavelength of ~260 m. The growth rates increase as μ is decreased. The e-folding times of the fastest-growing linear modes for beach 1 are 3.5, 5.7, 10.0, and 20.7 min. For the high friction case, $\mu = 0.00145$ m s^{-1}, unstable modes are predicted for wavelengths between 190 and 472 m, while the low friction case, $\mu = 0.00060$ m s^{-1}, has positive growth rates for a larger range of wavelengths be-

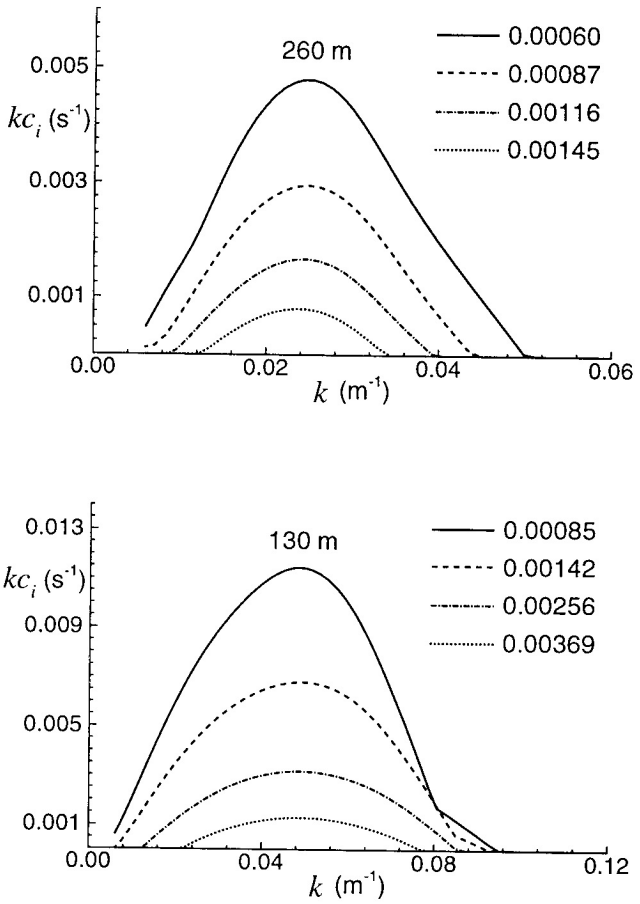

Figure 3. Results of the linear stability calculations for the alongshore velocity $v = V_{\mathrm{TGE}}(x)$ in terms of growth rate kc_i versus alongshore wavenumber k for (top) beach 1 and (bottom) beach 2 at different values of μ (m s^{-1}). The values of the wavelength $\lambda = 2\pi/k$ m at the maximum growth rate are indicated.

Table 1. Parameters From Experiments on Beaches 1 and 2

Beach	μ, m s^{-1}	Q	$\frac{\Delta Q}{Q_C}$	$V_{\mathrm{TGE}m}$, m s^{-1}	$< v >_m$, m s^{-1}	c_0, m s^{-1}
1	0.00145	0.1809	0.364	0.5822	0.4827	0.2686
1	0.00116	0.1158	0.593	0.7277	0.5199	0.3062
1	0.00087	0.0665	0.766	0.9647	0.5919	0.4346
1	0.00060	0.0301	0.894	1.4490	0.7498	0.5463
2	0.00369	0.4382	0.408	0.3931	0.3298	0.1770
2	0.00256	0.2134	0.712	0.5600	0.3830	0.1880
2	0.00142	0.0676	0.909	0.9809	0.4943	0.2283
2	0.00085	0.0250	0.966	1.5875	0.6512	0.4583

The bottom friction coefficient μ, the governing dimensionless parameter Q (4), $\Delta Q/Q_C = (Q_C - Q)/Q_C$, the maximum of the forcing profile $V_{\mathrm{TGE}m}$, the maximum of the observed time-averaged alongshore current $\langle v \rangle_m$, and the observed alongshore propagation velocity c_0.

tween 126 and ~1000 m. For $\mu \geq \mu_C = 0.00182$ m s^{-1} the flow is linearly stable. We denote the corresponding critical value of Q as Q_C, such that for $Q \geq Q_C$ the flow is linearly stable.

The growth rates for beach 2 are presented in Figure 3 (bottom). The values of μ used on beach 2 are significantly higher than those used on beach 1 because in this case the profiles are more unstable, so that $\mu_C = 0.00482$ m s^{-1} is approximately a factor of 2.6 greater than beach 1. The e-folding times of the fastest-growing modes for beach 2 are 1.5, 2.5, 5.3, and 12.9 min for these values of μ. The fastest-growing linear modes have alongshore wavelengths of 130 m for all values of μ.

Parameters for the experiments on both beaches are presented in Table 1. The ratio $\Delta Q/Q_C = (Q_C - Q)/Q_C$ gives a measure of how far from the critical stability condition the experiments are conducted. We note that the range of values for $\Delta Q/Q_C$ is similar for each beach.

The numerical experiments are started with the fluid at rest and run for 20 hours duration. Time series of the across-shore velocity u at a location 125 m offshore for beach 1 are shown in Figure 4. For $\mu = 0.00145$ m s^{-1}, fluctuations develop into a regular pattern of oscillations with an amplitude of about 0.13 m s^{-1} after a time of approximately $t = 6$ hours. The regularity of the fluctuations corresponds, as will be shown, to periodic wave-like behavior. As the bottom friction coefficient μ is decreased, the amplitudes and frequencies of the oscillations in the u time series increase, and the fluctuations become more irregular.

Time series of the u velocity for experiments on beach 2 at $x = 100$ m are shown in Figure 5 . The experiments again cover the range from regular to strongly irregular oscillations. Above a frictional value of $\mu = \mu_C = 0.00482$ m s^{-1} the flow is stable, and no fluctuations are observed. The magnitude of the regular fluctuations in u for $\mu = 0.00369$ m s^{-1} is ~0.07 m s^{-1}. For the more irregular cases at lower values of μ, there appears to be an asymmetry to the fluctuations. The positive (offshore) velocities have greater magnitudes than the negative (onshore) velocities. The time mean of the u time series is near zero as expected from continuity for a homogeneous flow. The asymmetry in the fluctuations shows stronger offshore current fluctuations, localized in time, compensated for by longer periods of weaker onshore flow.

Note from Figure 4 that the observable growth of the disturbances occurs at later times for the higher

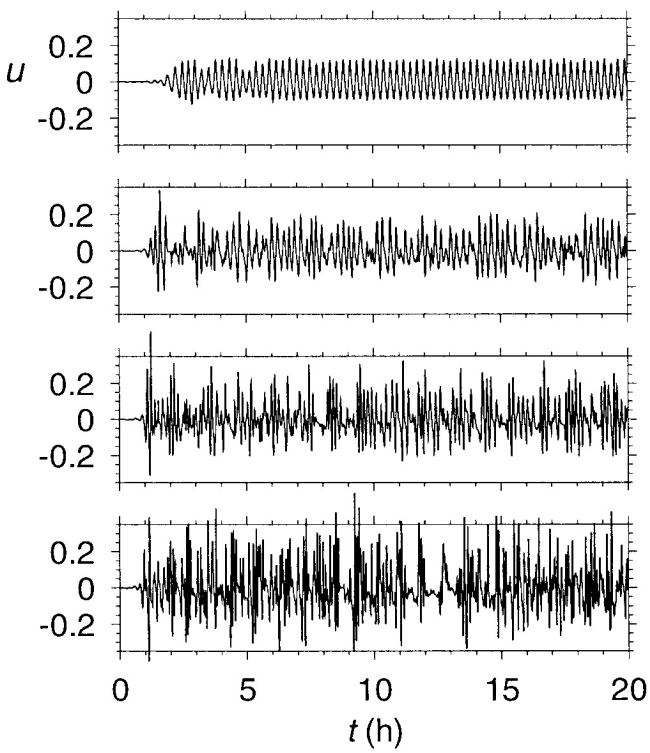

Figure 4. Time series of across-shore velocity component $u(x_0, y_0, t)$ (m s^{-1}) at $x_0 = 125$ m, $y_0 = 0$ from experiments on beach 1 with different values of μ from top to bottom $\mu = 0.00145$, 0.00116, 0.00087, and 0.00060 m s^{-1}.

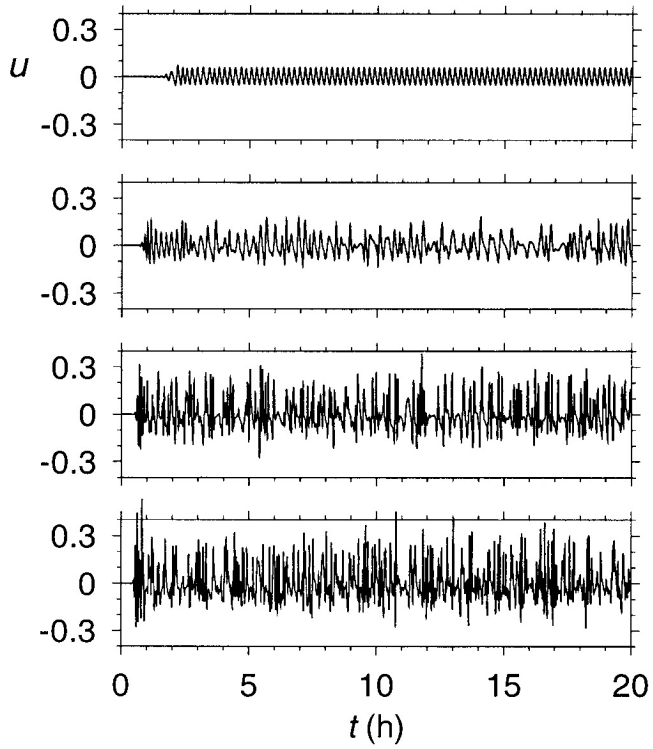

Figure 5. Time series of across-shore velocity component $u(x_0, y_0, t)$ (m s^{-1}) at $x_0 = 100$ m, $y_0 = 0$ from experiments on beach 2 with different values of μ from top to bottom $\mu = 0.00369$, 0.00256, 0.00142, and 0.00085 m s^{-1}.

frictional cases as expected from the results of the linear stability analysis. In general, at a fixed μ the time of initial observable growth of the instabilities depends on the amplitude of the forcing perturbations (8), with shorter times found for larger amplitude perturbations. This dependence is illustrated on beach 1 for $\mu = 0.00087$ m s^{-1} by time series of the across-shore and alongshore velocities for values of $\epsilon = 10^{-3}$ and 10^{-1} for $t < 5$ hours in Figure 6. In the experiment with $\epsilon = 10^{-3}$ (as in Figure 4) it takes ~1 hour for the disturbances to create across-shore velocities >0.05 m s^{-1}. For $\epsilon = 10^{-1}$ the across-shore velocities reach this threshold in ~30 min. Time series of the alongshore velocities at the same location indicate that the fluctuations begin after v has reached a value of ~0.5 m s^{-1}, which takes ~30 min under these forcing conditions. Since the time of development of the instabilities depends on the perturbations present, we do not attach particular significance to the initial flow behavior. Additional details of the flow development during periods of initial linear growth are presented in Appendix D.

The vorticity fields from experiments over beach 1 at $t = 15.3$ hours and beach 2 at $t = 10$ hours are shown in Plate 1. The $\mu = 0.00145$ m s^{-1} experiment shows a very regular pattern with five positive vortices in the alongshore direction centered ~90 m offshore. The positive vortices have an across-shore dimension of ~100 m, spanning the region from the bottom of the trough at $x = 43$ m to approximately $x = 140$ m, which is offshore of the crest of the sandbar and the maxima of V_{TGE}. The alongshore length scale for these vortices is 256 m, close to the length scale predicted for the fastest-growing unstable linear mode in Figure 3. The vortices maintain their coherent structure and propagate alongshore at a constant phase velocity $c_0 = 0.2686$ m s^{-1} determined, e.g., from the wavelength and period of the regular fluctuations in the u time series (Figure 4). We describe this type of flow behavior as an equilibrated shear wave. In this experiment, when the waves reach finite amplitude, they adjust the time mean current in a manner that stabilizes the flow as discussed in more detail in section 3.3.

In the second experiment, with $\mu = 0.00116$ m s^{-1}, a pair of vortices of opposite sign (loosely termed dipoles, even though the vortices are of finite size and possibly of unequal strength) located offshore at $x = 300$ m and $y = 200$ m are evident. Except for this localized disturbance the nearshore jet is similar to but slightly more irregular than the $\mu = 0.00145$ m s^{-1} case, with coherent alongshore propagating vortices over the sandbar and in the trough. Again, there are five clearly discernible vortices located over the sandbar, but in this case the positive vortices are observed to pulsate, stretch, catch up, and merge with one another. Occasionally, vortices will break away from the alongshore current and move offshore.

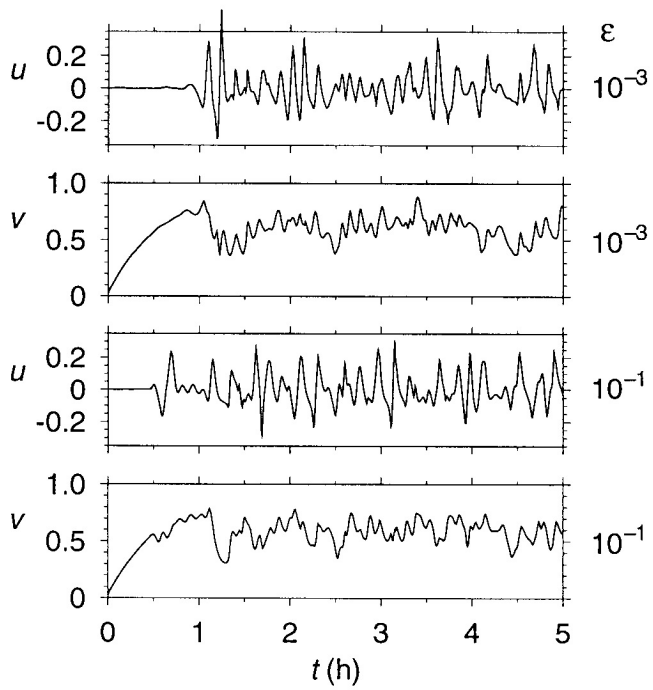

Figure 6. Time series of across-shore velocity component $u(x_0, y_0, t)$ (m s^{-1}) and alongshore velocity component $v(x_0, y_0, t)$ (m s^{-1}) at $x_0 = 125$ m, $y_0 = 0$ from experiments on beach 1 for $\mu = 0.00087$ m s^{-1} with different values of the perturbation amplitudes in (8), $\epsilon = 10^{-3}$ and 10^{-1}. Note the difference in scale for u and v.

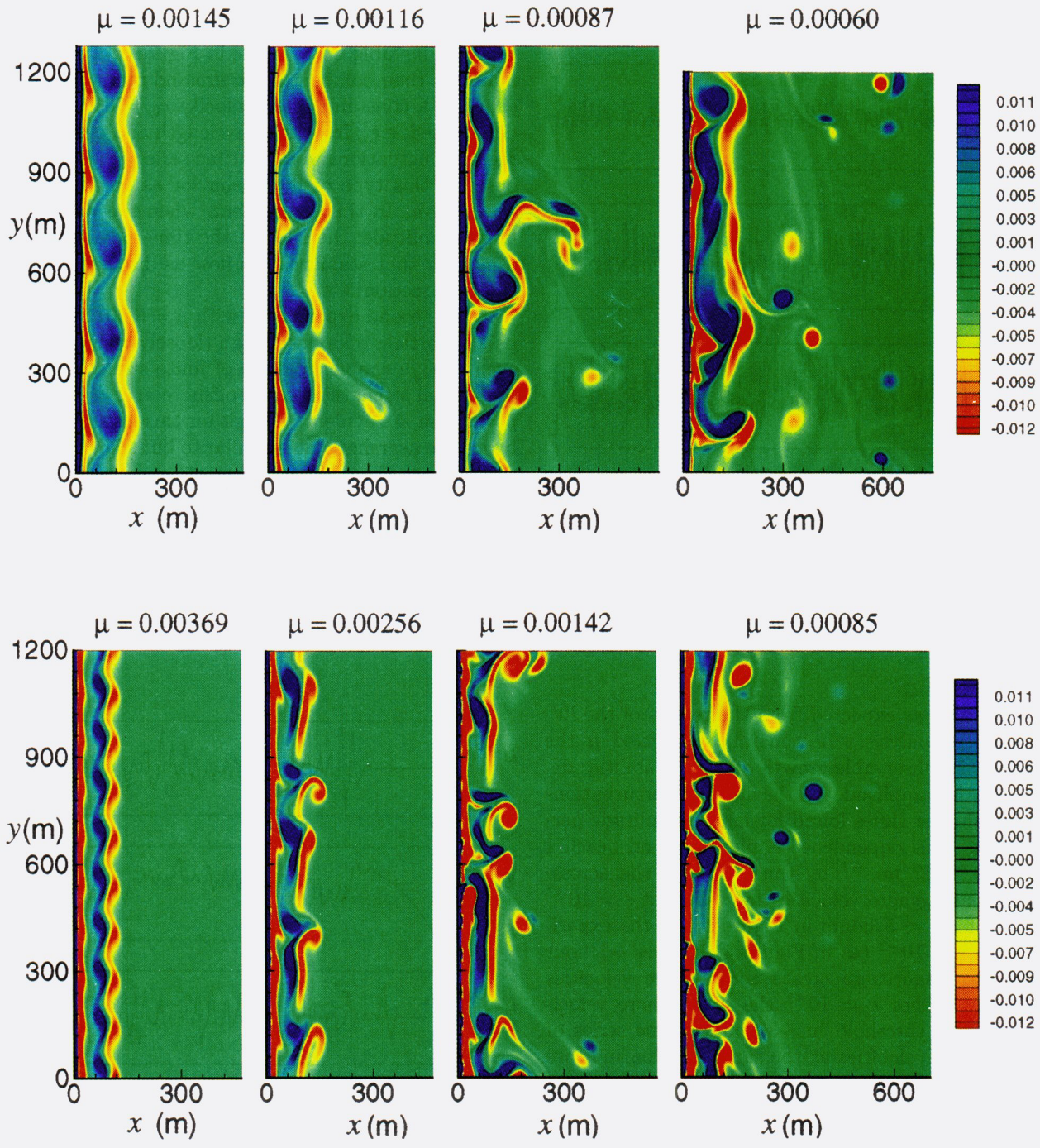

Plate 1. Contour plots of vorticity $\zeta(x, y, t)$ (s^{-1}) fields at $t = 15.3$ hours for experiments on (top) beach 1 and at $t = 10$ hours for experiments on (bottom) beach 2 with different values of μ ($m\ s^{-1}$). The blue contours indicate positive vorticity, yellow and red regions represent negative vorticity, and the green background regions have near-zero vorticity.

For the lower friction cases ($\mu = 0.00087$ and 0.00060 m s^{-1}) the vorticity fields become progressively more complex. There is an increased rate of vorticity shedding from the alongshore current. Frequently, the shedding involves vorticity of both signs, which detach into dipole structures. The dipoles are observed to propagate offshore and reach distances of 400–750 m from the coast. In addition, the vortex structures in the alongshore jet have become more disorganized but retain length scales of ~250 m.

For the lowest frictional case, $\mu = 0.00060$ m s^{-1}, the region outside of the sandbar from $x = 250 - 750$ m contains an energetic eddy field created by eddies shed from the alongshore currents. The eddies persist for ~1–2 hours, which is consistent with a frictional timescale $t_F = h/\mu$ in the range $42 \leq t_F \leq 139$ min for $1.5 \leq h \leq 5.0$ m. It is common for eddies with positive vorticity (blue) to appear to last longer than eddies with negative vorticity. This feature is apparently related to the fact that the central peak of the V_{TGE} jet has stronger positive vorticity in the region between $60 < x < 125$ m than negative vorticity in the region between $125 < x < 170$ m (Figure 2.) This asymmetry evidently contributes to making the positive vortices shed from the jet generally stronger than the negative ones, thus leading to the impression of greater persistence. The $\mu = 0.00060$ m s^{-1} case has the appearance of a turbulent shear flow. The alongshore length scales in the nearshore region $50 < x < 200$ m are difficult to characterize visually, but the flow appears to retain energy around the 250 m scale found to dominate at the higher values of μ.

Instantaneous vorticity fields from the experiments over beach 2 at $t = 10$ hours are shown in Plate 1 (bottom). For values of $\mu > \mu_C = 0.00482$ m s^{-1} the flows are linearly stable and no waves develop. At $\mu = 0.00369$ m s^{-1} the flow develops into a propagating equilibrated shear wave with alongshore wavelength of 133 m. The phase speed of the waves is $c_0 = 0.177$ m s^{-1}. Equilibrated flows of this type are established for frictional values between approximately $0.0033 < \mu < 0.0043$ m s^{-1}. Transition to more irregular flows occurs gradually near $\mu = 0.0033$ m s^{-1}.

For $\mu = 0.00256$ m s^{-1} the vorticity field in Plate 1 shows propagating disturbances with longer wavelengths of about 200–300 m. These features remain confined to the outer region of the current, where they form fronts of vorticity, roll up, and sometimes merge with the disturbances in front or behind in an irregular manner. This behavior is reminiscent of that found over plane beaches by *Allen et al.* [1996].

At the lower frictional values, $\mu = 0.00142$ and 0.00085 m s^{-1}, the vorticity fields become progressively more complex and resemble turbulent shear flows in which eddies are formed in an unsteady manner and either propagate alongshore or break away from the current and move offshore of the sandbar. For $\mu = 0.00142$ m s^{-1} an offshore propagating dipole may be seen at approximately $(x, y) = (400, 100)$ m. In the experiment with $\mu = 0.00085$ m s^{-1} the nearshore region is populated with energetic eddies. An event has just occurred at $(x, y) = (400, 800)$ m where a positive (blue) vortex has "sheared out" and destroyed its weaker companion negative (red) vortex, creating a weakly negative (yellow) circle around the core of positive vorticity. This process is frequently observed in the experiments and occurs when the weaker member of an offshore propagating dipole is elongated by the shear from its partner of opposite sign. When this occurs, offshore propagation stops and the remaining vortex spins down from bottom friction with little change in position unless another vortex approaches close enough (≃100 m) to interact. Often, opposite-signed vortices in the offshore region set one another in motion, propagating along curved paths if they are of unequal strength. Occasionally, two vortices of the same sign will orbit one another or merge to form a stronger vortex.

The vorticity fields from experiments on beaches 1 and 2 in Plate 1 show that there are several different flow regimes that can develop from nonlinear instabilities of alongshore currents. Four general categories of flows that develop include (1) equilibrated shear waves, (2) fluctuating eddies confined to the current, (3) fluctuating eddies that are primarily confined to the current but with some eddies that break away from the alongshore jet, and (4) a turbulent shear flow in which the energetic eddy field in the alongshore current fills the nearshore region and continuously sheds eddies that populate a region offshore of the sandbar. Similar qualitative results are found for both beaches 1 and 2 and also in additional experiments not presented here with other beach bathymetries, alongshore domain lengths, and/or wave field forcing conditions. Thus the qualitative nature of resulting flows appears to be robust for barred beaches with forcing from the *Thornton and Guza* [1986] submodel and appears to be independent of the specific beach profile used in the model.

3.2. Flow Properties

The time- and alongshore-averaged perturbation kinetic energy $\mathrm{KE} = \frac{1}{2}\langle \widetilde{u}^2 + \widetilde{v}^2 \rangle$ for experiments over beach 1 and beach 2 are shown in Figure 7 as a function of x. For the cases with the lowest bottom friction, $\mu = 0.00060$ m s^{-1} (beach 1) and $\mu = 0.00085$ m s^{-1} (beach 2), significant perturbation energy extends beyond 500 m offshore. For the equilibrated shear wave cases (largest μ values) the perturbation energy is confined within the region of forcing of the alongshore jets (within 175 and 125 m of the shore). Note that for beach 2, there is very little perturbation kinetic energy in the inshore region $x < 40$ m. In general, as the bottom friction decreases, the kinetic energy in the perturbations increases, and the distribution broadens and spreads offshore. The maxima of perturbation kinetic energy generally occur at the location of strongest mean alongshore velocities, i.e., at $x = 80$–90 m.

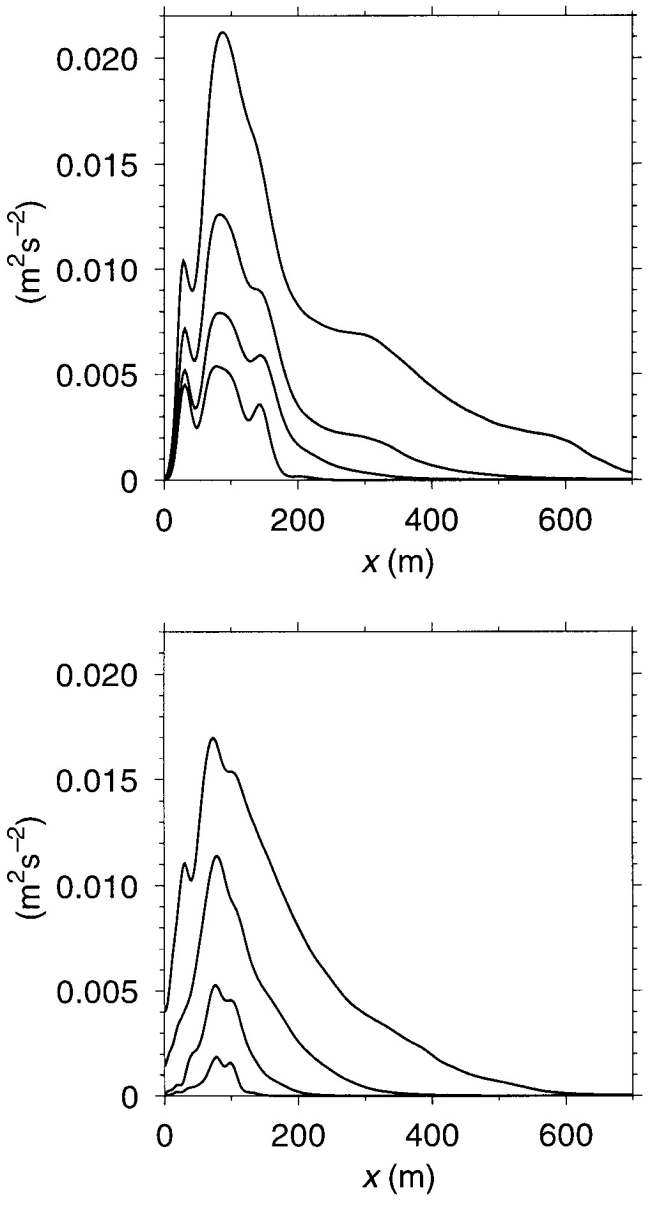

Figure 7. Alongshore- and time-averaged perturbation kinetic energy density $0.5\langle\overline{\tilde{u}^2}+\overline{\tilde{v}^2}\rangle$ as a function of x for (top) beach 1 with $\mu = 0.00145$, 0.00116, 0.00087, and 0.00060 m s^{-1} and for (bottom) beach 2 μ =0.00369, 0.00256, 0.00142, and 0.00085 m s^{-1} where the energy density increases with decreasing μ. The time averages are for 12 hours from $t = 8$ to 20 hours.

The differences between the equilibrated shear wave regime and the progressively more unsteady cases at lower friction are illustrated by the alongshore wavenumber-frequency spectra of the across-shore and alongshore velocities in Figures 8 and 9. The spectra in Figures 8 and 9 are calculated from $u(x_0, y, t)$ and $v(x_0, y, t)$ where the offshore location x_0 (specified in the captions for Figures 8 and 9) is generally close to the location of the maximum of V_{TGE}. We examine the u spectra from the beach 1 experiment in Figure 8 first. For the highest friction $\mu = 0.00145$ m s^{-1}, the energy is strongly localized at the point $(k, \omega) =$ (0.0245 m^{-1}, 0.0066 s^{-1}). Approximately 2 orders of magnitude more energy are found at this (k, ω) point than at any other point. The corresponding wavelength, $\lambda = 2\pi/k = 256$ m, and the period $T = 2\pi/\omega = 953$ s. This wavelength agrees with the estimate from the vorticity field in Plate 1, which shows five disturbances with alongshore length scales of 256 m each, and this period agrees with that estimated from the u time series in Figure 4. Note, additionally, that there is also a local energy maxima at $(k, \omega) = (0.049$ m^{-1}, 0.0132 s$^{-1})$ corresponding to twice the (k, ω) values of the maximum in energy. For the lower friction cases the spectra show progressive spreading of the energy to higher and lower wavenumbers and frequencies. For $\mu =$ 0.00116 m s^{-1}, with larger fluctuations, the energy is in a fairly narrow band, around the line $\omega = 0.30k$, suggestive of nondispersive waves moving at the phase speed $c_0 = 0.30$ m s^{-1}. For the two lowest friction experiments the energy is spread to higher wave numbers and to higher frequencies. The energy is still concentrated about a line representing a linear relation between ω and k but fills a wider band about that line. The (k, ω) points of maximum energy for $\mu =$ 0.00116, 0.00087, and 0.00060 m s^{-1} are (0.0196 m^{-1}, 0.0060 s^{-1}), (0.0196 m^{-1}, 0.0085 s^{-1}), and (0.0209 m^{-1}, 0.0114 s^{-1}), respectively.

The dominant phase speeds of alongshore propagation ($c_0 = \omega/k$) can be estimated by utilizing the (k, ω) points of maximum energy. For the highest friction case $\mu = 0.00145$ m s^{-1}, the phase speed of the most energetic mode is 0.269 m s^{-1} which agrees with the previous estimate. Details of the dominant phase speeds from each of the cases and their relationships to the mean velocities are discussed in section 3.3.

The $v(x_0, y, t)$ spectra (Figure 8, bottom) for experiments on beach 1 include similar distribution of energy to the u spectra with two main differences. First, the v spectra contain energy maxima at $k = 0$ owing to contributions from $\overline{v}$ not present in u and correspondingly higher energy at low values of k and ω. Second, at higher k and ω the v spectral levels are not as large as those of u.

To examine the effect of the alongshore domain length $L^{(y)}$ on the flow, additional experiments were run with $L^{(y)} = 2560$ and 2400 m for bottom friction coefficients of $\mu = 0.00087$ $^{-1}$ and 0.00060 m s^{-1}, respectively. These experiments produce results essentially equivalent to those obtained with $L^{(y)} = 1280$ and 1200 m. In particular, the resulting (ω, k) spectra for $u(x_0, y, t)$ and $v(x_0, y, t)$ are nearly identical to those shown in Figure 8. In an additional experiment with $\mu = 0.00145$ m s^{-1} and $L^{(y)} = 1920$ m, the flow develops into seven equilibrated waves with wavelengths of 274 m. This wavelength corresponds to the integral value nearest to that of the fastest-growing linear mode (Figure 3). We conclude that the important flow characteristics found in the basic experiments with $L^{(y)} = 1280$ and 1200 m are independent of the choice of $L^{(y)}$.

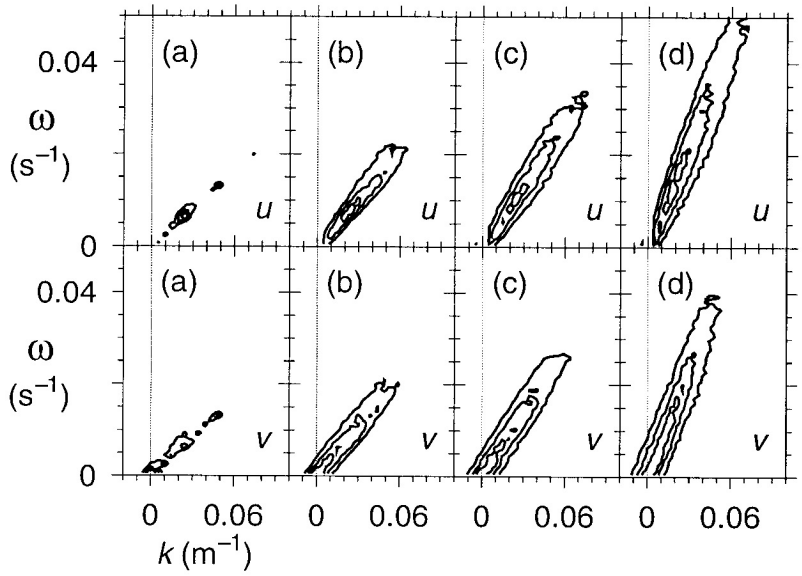

Figure 8. Alongshore wavenumber-frequency (k, ω) spectra for (top) the across-shore velocity $u(x_0, y, t)$ and for (bottom) the alongshore velocity $v(x_0, y, t)$ from experiments on beach 1 with the following values of μ: 0.00145 (case a), 0.00116 (case b), 0.00087 (case c), and 0.00060 (case d) m s^{-1}. The spectra are calculated utilizing Fourier transforms in y and t for an 18 hour portion of the experiments (from t = 2 to 20 hours) at the offshore location x_0 = 125 m for the first three cases and at x_0 = 100 m for the case of μ = 0.00060 m s^{-1}. The spectra are calculated using a cosine taper on the first and last 10% of the time series, and the resulting spectra are band averaged over 10 frequencies. The contour levels are 10^{-1}, 10^{0}, and 10^{1} m^2 s^{-2}.

The wavenumber-frequency spectra for experiments with beach 2 are shown in Figure 9. The results are similar to those from beach 1. At high friction μ = 0.00369 m s^{-1}, nearly all of the energy is concentrated near a single frequency, ω = 0.0083 s^{-1}, with some energy also evident at the first harmonic, ω = 0.016 s^{-1}. As for beach 1, at the lower frictions the energy is spread to higher wave numbers and to higher frequencies but is still concentrated about a line representing a linear relation between ω and k. Note that the vertical axis

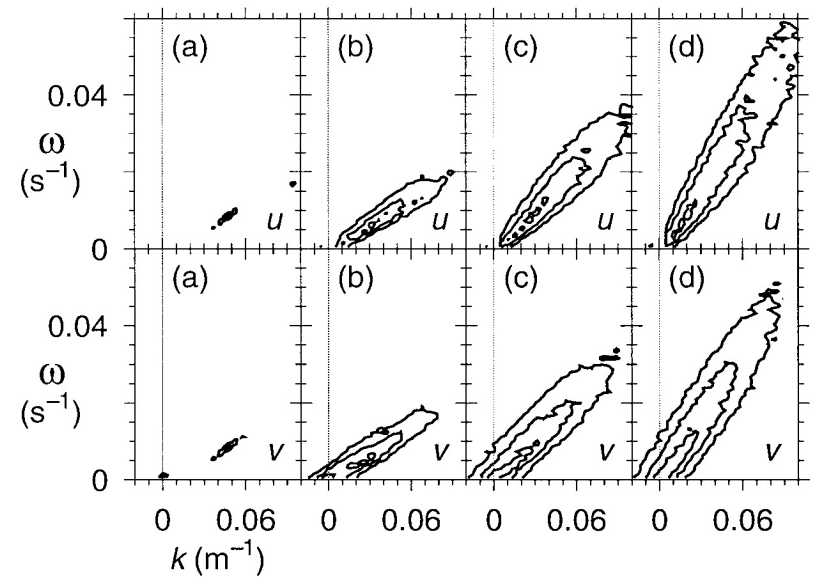

Figure 9. Alongshore wavenumber-frequency (k, ω) spectra for (top) the across-shore velocity $u(x_0, y, t)$ and for (bottom) the alongshore velocity $v(x_0, y, t)$ from experiments on beach 2 with the following values of μ: 0.00369 (case a), 0.00256 (case b), 0.00142 (case c), and 0.00085 (case d) m s^{-1}. The spectra are calculated as in Figure 8 for an 18 hour portion of the experiments (from t = 2 to 20 hours) at the offshore location x_0 = 100 m. The contour levels are 10^{-1}, 10^{0}, and 10^{1} m^2 s^{-2}.

extends to higher frequencies for beach 2 than for beach 1. The (k, ω) points containing maximum energy for $\mu = 0.00369$, 0.00256, 0.00142, and 0.00085 m s^{-1} are (0.0471 m^{-1}, 0.0083 s^{-1}), (0.0314 m^{-1}, 0.0059 s^{-1}), (0.0157 m^{-1}, 0.0036 s^{-1}), and (0.0209 m^{-1}, 0.0096 s^{-1}), respectively.

The $v(x_0, y, t)$ wavenumber-frequency spectra for experiments on beach 2 show the same trends as for beach 1. The energy in v is concentrated about the same band, $c_0 = \omega/k$, as for u but with maxima at $(k, \omega) = (0, 0)$.

To examine the effect of the choice of x_0 on the estimate of $c_0 = \omega/k$, alongshore wavenumber-frequency spectra from the vorticity fields were calculated for different across-shore positions between $10 < x_0 < 250$ m. The resulting estimates for c_0 are remarkably independent of x_0 and of the local mean velocities $\langle \overline{v} \rangle$. This evidently reflects the basic propagating nature of the fluctuations as waves, even in the more turbulent cases.

The time mean velocity profiles $\langle v \rangle$ at $y = L^{(y)}/2$ from a 15 hour portion of the experiments ($5 < t < 20$ h) are compared with the velocity profiles V_{TGE} for the experiments with $\mu = 0.00145$ and 0.00060 m s^{-1} on beach 1 in Figure 10. In both cases the mean velocity profiles $\langle v \rangle$ are broader and their maxima are smaller than the forcing profiles V_{TGE}. In the high friction case the mean alongshore current has a maximum value of $\langle v \rangle_M = 0.50$ m s^{-1} compared to the maximum V_{TGE} value of 0.60 m s^{-1}. In the low friction case the difference is more dramatic. In the absence of nonlinear dynamics, the forced velocity profile V_{TGE} would achieve a frictionally balanced maximum velocity of 1.45 m s^{-1}, but the observed maximum mean velocity $\langle v \rangle_M$ is closer to 0.7 m s^{-1}. For the lower friction experiment, $\mu = 0.00060$ m s^{-1}, a significant feature is the filling in of the velocity deficit between the two jets of the alongshore current in the trough located at approximately $x = 50$ m. This is one of the principle results from these experiments. An effect of the finite-amplitude shear instabilities is to spread the mean alongshore momentum from regions of surface wave breaking, as parameterized in the (T-G) model, into the trough region of relatively low surface wave breaking.

Also pictured in Figure 10 are the time-averaged (15 hours) rms velocity fluctuations $u_{\mathrm{rms}} = \langle u'^2 \rangle^{1/2}$ and $v_{\mathrm{rms}} = \langle v'^2 \rangle^{1/2}$ as a function of x at $y = L^{(y)}/2$. For the equilibrated shear wave case, $\mu = 0.00145$ m s^{-1}, the fluctuations occur inside of $x = 200$ m and have magnitudes of $\sim$0.1 m s^{-1}. For the more turbulent case, $\mu = 0.00060$ m s^{-1}, substantial velocity fluctuations extend out to $x = 700$ m. For $x > 500$ m the fluctuations exceed the mean velocity. Inside of 200 m the velocity fluctuations have magnitudes of $\sim$0.15 m s^{-1}, which is roughly one quarter of the mean velocity in this region.

Similar results for beach 2 are shown in Figure 11. There is very little difference between the mean $\langle v \rangle$ and forced V_{TGE} alongshore velocity profiles for the experiment with the strongest friction, $\mu = 0.00369$ m s^{-1}.

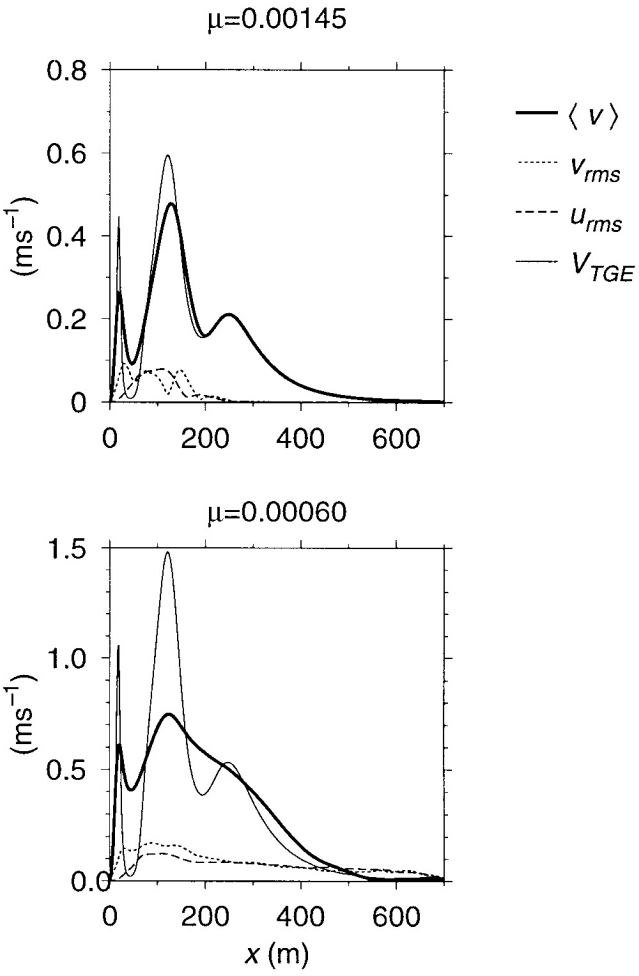

Figure 10. Time-averaged alongshore currents $\langle v \rangle$ at $y = L^{(y)}/2$ and the forcing velocity profiles V_{TGE} as a function of x from experiments on beach 1 with $\mu = 0.00145$ and 0.00060 m s^{-1}. Also shown are the rms velocities $u_{\mathrm{rms}} = \langle u'^2 \rangle^{1/2}$ and $v_{\mathrm{rms}} = \langle v'^2 \rangle^{1/2}$ at $y = L^{(y)}/2$.

There are small fluctuations u_{rms} and v_{rms} in the inner jet, but the mean velocity is close to the forced velocity. This corresponds to the previous observation that the velocity fluctuations result from small-amplitude equilibrated shear waves. It is clear from Figure 11 that these equilibrated shear waves do not significantly fill in the alongshore velocity profile in the trough. For the experiment at low friction, $\mu = 0.00085$ m s^{-1}, the alongshore momentum input from the forcing is effectively diffused from the region of the sandbar into the trough and offshore of the bar. The mean velocities in the trough are $\sim$80% of the mean velocities over the sandbar. Inshore of 40 m, the mean jet is less affected by the fluctuations, perhaps because the water is shallower and motions are more strongly damped by the bottom friction. In the regions of the trough and bar the rms perturbation velocities are again approximately one quarter of the amplitude of the mean currents.

The terms from the time and alongshore averaged y momentum balance (18) are plotted for beach 1 in Fig-

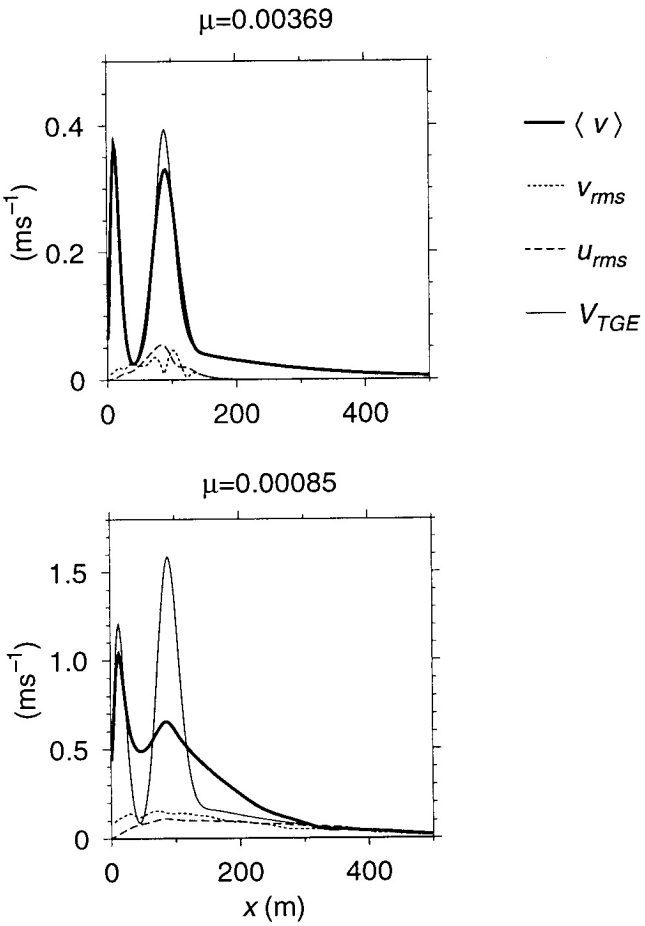

Figure 11. Time-averaged alongshore currents $\langle v \rangle$ at $y = L^{(y)}/2$ and the forcing velocity profiles V_{TGE} as a function of x from experiments on beach 2 with μ = 0.00369 and 0.00085 m s^{-1}. Also shown are the rms velocities $u_{\mathrm{rms}} = \langle u'^2 \rangle^{1/2}$ and $v_{\mathrm{rms}} = \langle v'^2 \rangle^{1/2}$ at $y = L^{(y)}/2$.

ure 12. The terms show that the difference in velocity between the mean and the forced profiles, $\mu \langle \overline{v} - V_{\mathrm{TGE}} \rangle$, is balanced by the gradient of the Reynolds stress $\langle \overline{(huv)_x} \rangle = \langle \overline{(h\tilde{u}\tilde{v})_x} \rangle$. The Reynolds stress term represents the alongshore- and time-averaged across-shore flux of perturbation alongshore velocity $\tilde{v}$. It is noteworthy that the difference in the mean y momentum balance between the equilibrated shear wave case (μ = 0.00145 m s^{-1}) and the turbulent case (μ = 0.00060 m s^{-1}) is primarily quantitative rather than qualitative in spite of the large differences in the qualitative characteristics of the flows in these experiments.

Inside of 40 m, diffusion by the biharmonic friction contributes to the momentum balance as a result of the large gradients in V_{TGE} and $\langle \overline{v} \rangle$ near the coast. For $x > 40$ m, biharmonic friction plays essentially no role in the momentum balance. The residual term is the sum of the other terms in the equation and is relatively small. It would be expected to be zero for a long enough time average or y average over a statistically steady and homogeneous flow. In these experiments, averaged in time over 12 hours and in y over $L^{(y)}$, this assumption is approximately satisfied.

The real part of the alongshore wavenumber-frequency cross spectra calculated from $u(x_0, y, t)$ and $v(x_0, y, t)$ for experiments on both beaches are shown in Figure 13 at the same offshore locations as for the u and v spectra in Figures 8 and 9. These spectra indicate the contributions from different wavenumbers and frequencies to the Reynolds stress $\langle \overline{huv} \rangle$, which is responsible for the across-shore exchange of alongshore momentum. The $\omega - k$ distributions in the real part of the cross spectra are generally similar to the $u(x_0, y, t)$ spectra in Figures 8 and 9 with an apparent shift of the larger spectral levels to somewhat lower values of ω and k, evidently reflecting the characteristics of the v spectra for small ω and k.

Time- and space-lagged correlations

$$C(y_L, t_L) = \frac{\langle u'(x_0, y_0 + y_L, t + t_L)\, u'(x_0, y_0, t) \rangle}{\langle u'^2(x_0, y_0 + y_L, t + t_L) \rangle^{1/2}\, \langle u'^2(x_0, y_0, t) \rangle^{1/2}}, \quad (20)$$

are presented in Plate 2 for μ = 0.00145, 0.00116, and 0.00060 m s^{-1} for beach 1 from time series of $u(x_0, y_0, t)$,

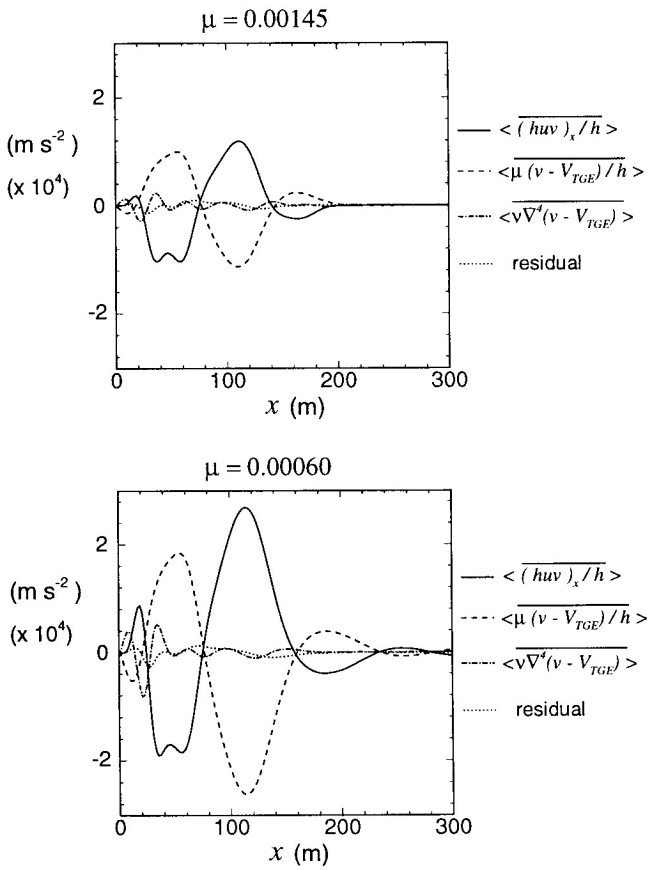

Figure 12. Terms in the time- and alongshore-averaged y momentum equation (18) as a function of x for beach 1 experiments with μ = 0.00145 and 0.00060 m s^{-1}. The time-averages are for 12 hours from t = 8 to 20 hours.

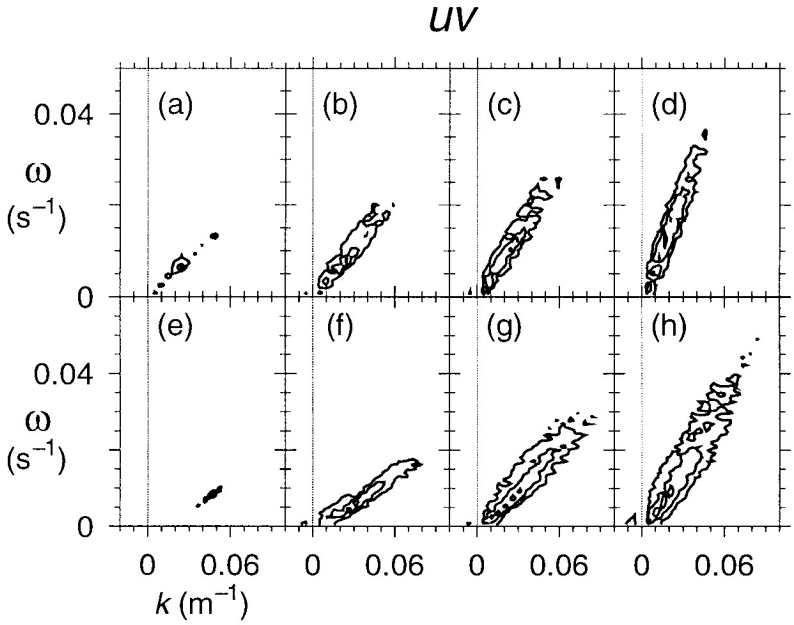

Figure 13. The real part of the alongshore wavenumber-frequency (k,ω) cross spectra of $u(x_0,y,t)$ and $v(x_0,y,t)$ from experiments on (top) beach 1 and (bottom) beach 2 with the following values of μ: 0.00145 (case a), 0.00116 (case b), 0.00087 (case c), 0.00060 (case d), 0.00369 (case e), 0.00256 (case f), 0.00142 (case g), and 0.00085 (case h) m s^{-1}. These spectra are calculated at the same locations and in the same manner as the u and v spectra in Figures 8 and 9. The contour levels are 10^{-1}, 10^{0}, and 10^{1} m^2 s^{-2}.

where x_0 is specified in the figure caption and $y_0 = 0$ m. For the $\mu = 0.00145$ m s^{-1} experiment the correlations indicate the wave-like nature of the flow. For example, on the line at $t_L = 0$ from $y_L = -640$ to 640 m the correlations oscillate in a regular fashion between values near -1 and 1 through five wavelengths. Approximately constant correlations exist along lines with slope $c_0 = y_L/t_L = 0.27$ m s^{-1}, indicating wave propagation at that velocity in close agreement with the estimate obtained previously from the wavenumber-frequency spectra of 0.269 m s^{-1}.

For the intermediate friction case, $\mu = 0.00116$ m s^{-1}, there is a similar high correlation extending diagonally along a line through the origin at $(y_L, t_L) = (0,0)$. The correlations outside of this center diagonal line are much weaker, with magnitudes <0.4, indicating the fact that this flow is more complex than uniform waves. Time and space correlation scales, determined simply as the lag to zero correlation along $y_L = 0$ and $t_L = 0$, respectively, give $t_C \approx 3.3$ min and $y_C \approx 66$ m. The time and space correlation scales calculated along the line of high correlation $c_0 = y_L/t_L = 0.31$ m s^{-1} are substantially larger. Determined by the lag to correlation of zero, these are $t_P \approx 100$ min and $y_P \approx 1900$ m. For the lowest frictional case, $\mu = 0.00060$, the results show decreased correlation scales of $t_C \approx 1.9$ min and $y_C \approx 64$ m. When considered along the line $c_0 = y_L/t_L = 0.55$ m s^{-1}, the correlation scales are $t_P \approx 27$ min and $y_P \approx 900$ m. These scales are also decreased relative to the values found in the experiments with larger μ. Similar results were obtained for beach 2. The decrease in correlation scales as μ decreases clearly illustrates the transition from equilibrated shear waves to a more turbulent shear flow.

The above results from the space- and time-lagged correlations lead us to analysis of the flow in a frame of reference that translates alongshore at the dominant propagation velocity c_0. The time mean vorticity fields $\langle\zeta(x,\eta)\rangle$ where $\eta = y - c_0 t$ are plotted in Plate 3 (top) for beach 1. For each value of bottom friction the alongshore propagation velocity c_0 is determined from the wavenumber frequency spectra. The velocities used are $c_0 = 0.269$, 0.306, 0.434, and 0.546 m s^{-1} in order of highest to lowest friction. The vorticity field in this translating coordinate system is averaged over a 10 hour period, from $t = 6.7$ to 16.7 hours, in the nearshore region $0 < x < 500$ m. The rms vorticity fluctuations $\zeta_{\rm rms} = \langle[\zeta(x,\eta) - \langle\zeta(x,\eta)\rangle]^2\rangle^{1/2}$ about the mean are shown in Plate 3 (bottom) for the same 10 hour period.

For $\mu = 0.00145$ m s^{-1} the time mean captures the coherent alongshore propagating structure of the vorticity field. There are five distinct alongshore wavelengths evident in the region of the strongest mean alongshore current, centered at approximately $x = 100$ m. The mean vorticity field in Plate 3 is very similar to the instantaneous vorticity field at $t = 15.3$ hours shown in Plate 1. The vorticity field in this experiment propagates at a nearly uniform velocity. The rms vorticity fluctuations (Plate 3, bottom) occur in a well-defined pattern around the perimeters of each of the five mean vortex structures, indicating that they fluctuate weakly in a regular manner as they propagate alongshore.

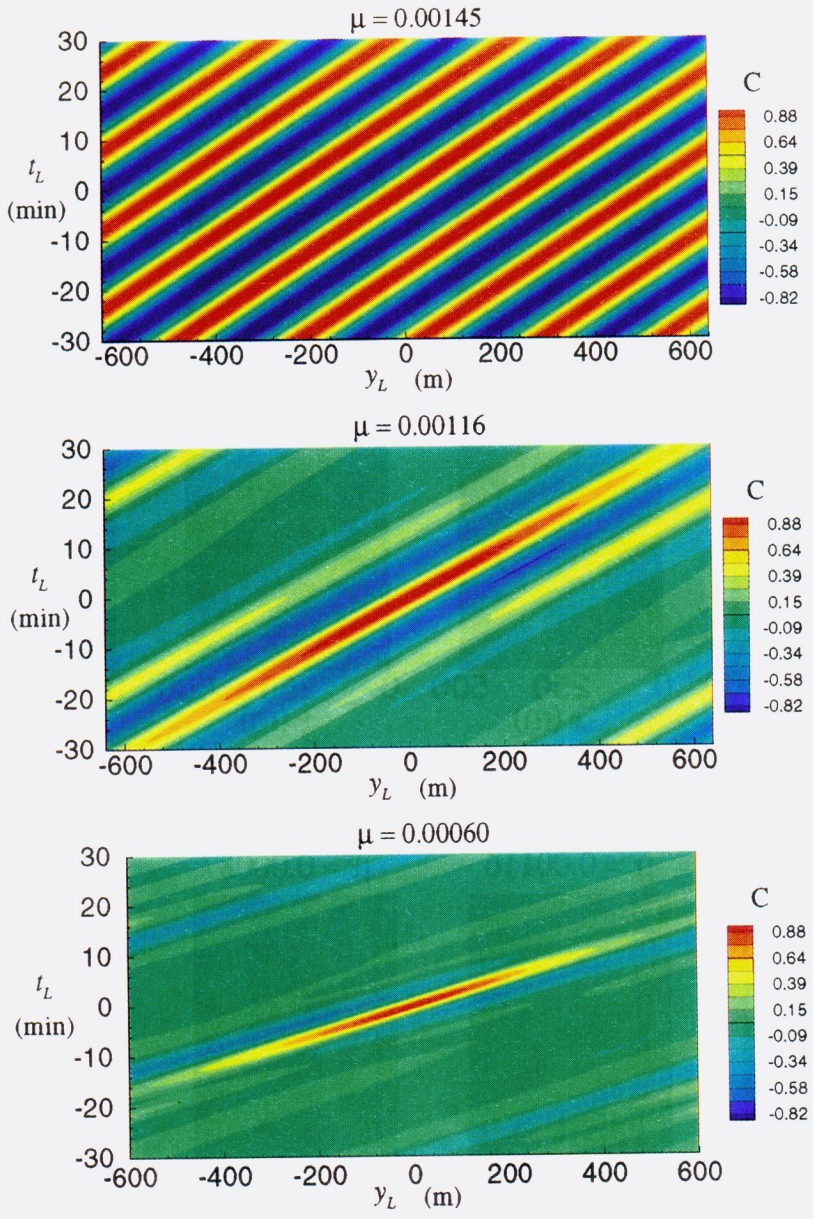

Plate 2. Time- and space-lagged correlations $C(y_L, t_L)$ (20) for the across-shore velocity component $u(x_0, y, t)$ from beach 1 experiments with different values of μ (m s^{-1}) ($x_0 = 125$ m for $\mu = 0.00145$ and 0.00116 m s^{-1}; $x_0 = 100$ m for $\mu = 0.00060$ m s^{-1}).

For the lower frictional experiments, coherent structures in the mean vorticity fields are less clearly defined, and the mean vorticity is more uniform in the alongshore direction. Nevertheless, the positive vorticity in the region $50 < x < 130$ m remains relatively strong and shows evidence of an approximate 250 m alongshore length scale. At the same time, the rms fluctuations become stronger and distributed over a larger spatial region. For $\mu = 0.00060$ m s^{-1} the region between $100 < x < 400$ m becomes dominated by offshore excursions of strong vortex dipole events that appear as streaks in the rms fields. Note also that there is a relative minimum in the rms fields located at approximately $x = 90$ m, where the mean vorticity is largest.

3.3. Alongshore Propagation

Results from application of linear stability analysis to the time- and alongshore-averaged velocity profiles $\langle \overline{v} \rangle$ are shown in Figure 14. Growth rates kc_i, as a function of wavenumber k, from the experiments for both beach 1 and beach 2 are plotted. For beach 1 the mean velocity profiles for $\mu = 0.00060$, 0.00087, and 0.00116 m s^{-1} are unstable, while the mean velocity profile for $\mu = 0.00145$ m s^{-1} is stable. We note first that the growth rates kc_i in Figure 14 are approximately an order of magnitude smaller than the growth rates shown in Figure 3 for the effective forcing velocity profiles V_{TGE}. The main points from Figure

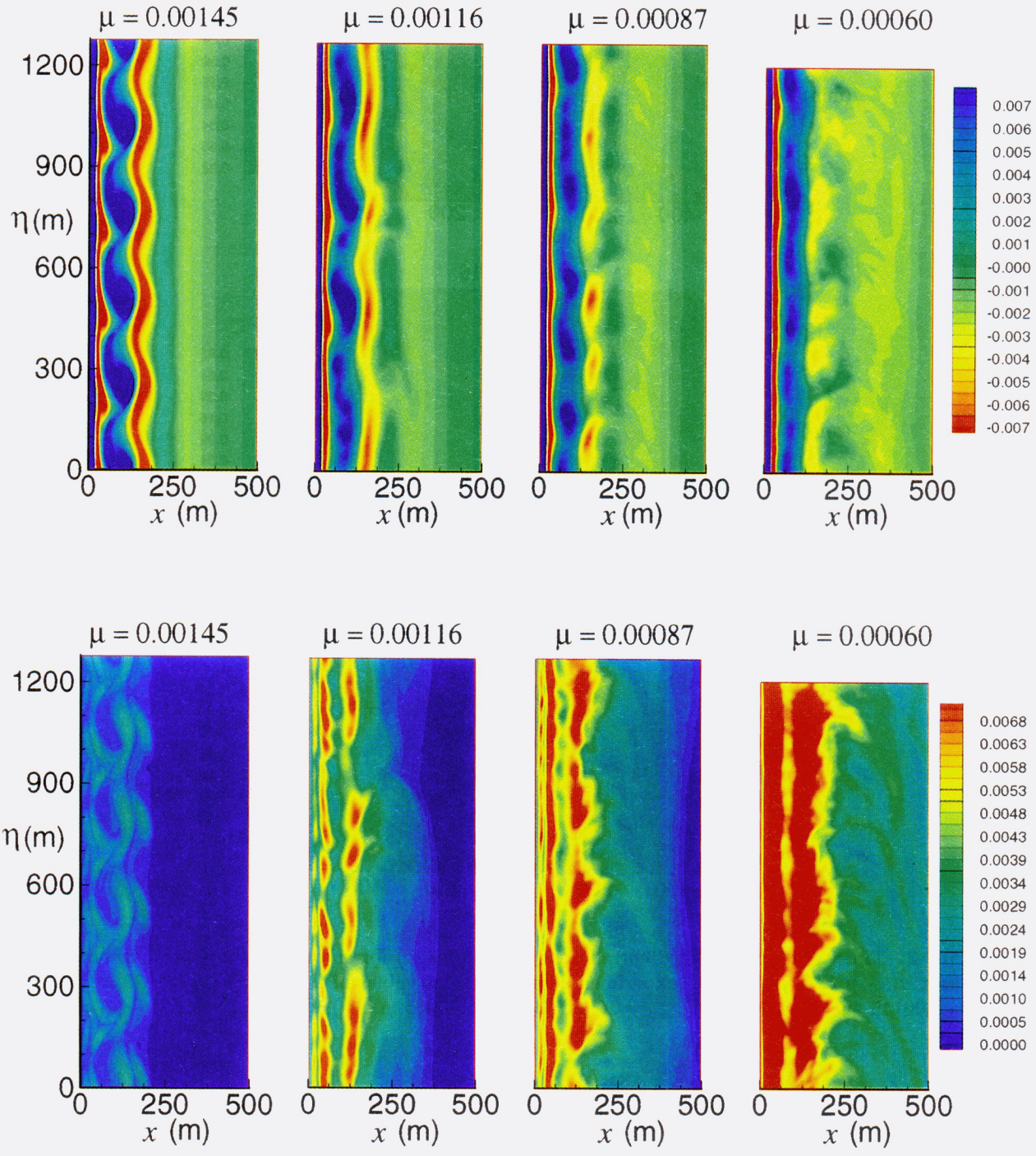

Plate 3. The (top) time-averaged vorticity $\langle\zeta(x,\eta)\rangle$ (s^{-1}) and the (bottom) rms vorticity fluctuations $\langle[\zeta(x,\eta,t)-\langle\zeta(x,\eta)\rangle]^2\rangle^{1/2}$ (s^{-1}) for beach 1 experiments with different values of μ ($m\ s^{-1}$) calculated in a frame of reference $\eta = y - c_0 t$ translating at the observed dominant alongshore propagation velocity c_0 calculated for each experiment from the (k,ω) spectra in Figure 8 as explained in the text. The time averages are for 10 hours from $t = 6.7$ to 16.7 hours.

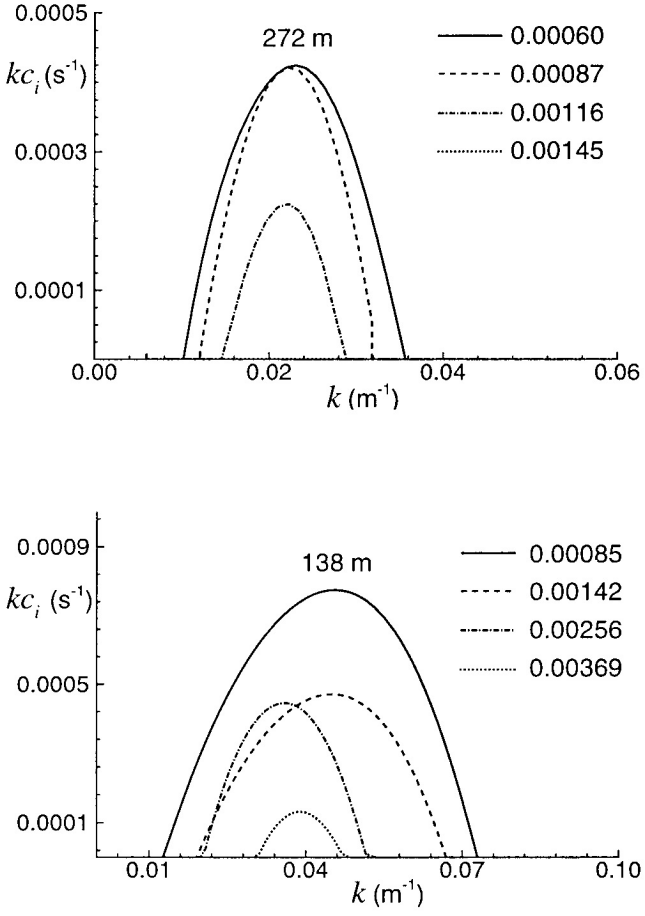

Figure 14. Results of the linear stability calculations for the time- and alongshore-averaged alongshore velocity $\langle\overline{v}\rangle$ in terms of growth rate kc_i versus alongshore wavenumber k for (top) beach 1 and (bottom) beach 2 at different values of μ (m s^{-1}). The values of the wavelength $\lambda = 2\pi/k$ m at the maximum growth rate are indicated.

14 for beach 1 are that the alongshore wavelengths predicted for the most unstable mode for the mean velocity profiles (272 to 283 m) are approximately the same as the alongshore wavelengths predicted for the most unstable modes for the forced velocity profiles V_{TGE} and are also close to the wavelengths obtained from the wavenumber-frequency spectra at the points of maximum energy.

For beach 2 the effective forcing profiles V_{TGE} (Figure 3) have fastest growth at wavelengths of about 130 m. This is similar to the results from the mean profiles $\langle\overline{v}\rangle$ in Figure 14 where the wavelengths range from 138 m for $\mu = 0.00085$ m s^{-1} to 176 m for $\mu = 0.00256$ m s^{-1}. The numerical experiments show that significant energy is contained at these wavelengths though the maximum energy in the wavenumber-frequency spectra are at generally greater alongshore wavelengths of 300, 400, and 200 m for $\mu = 0.00085$, 0.00142, and 0.00256 m s^{-1} respectively.

Linear stability analysis also gives values for the velocity of propagation c_r of the most unstable linear mode. Three values of propagation velocity are compared in Figure 15: the values found from linear stability analysis of V_{TGE} and of $\langle\overline{v}\rangle$ and the observed values c_0 found from the wavenumber-frequency (k,ω) spectra. Propagation velocities are not predicted from $\langle\overline{v}\rangle$ for $\mu = 0.00145$ m s^{-1} on beach 1 because linear theory did not predict unstable modes. For beach 1, propagation velocity predictions are similar for V_{TGE} and $\langle\overline{v}\rangle$ and both agree over the range of μ with the values of c_0 obtained from the (k,ω) spectra, even when V_{TGE} and $\langle\overline{v}\rangle$ differ substantially. For beach 2 the propagation velocities from the linear stability analysis of V_{TGE} and $\langle\overline{v}\rangle$ likewise do not differ greatly. The observed velocities c_0 agree well with the linear stability results from $\langle\overline{v}\rangle$ for $\mu \geq 0.00256$ m s^{-1}, but the agreement is not as good at smaller μ. We discuss these results further in the next section.

The ratio of the maximum of the mean alongshore velocity $\langle\overline{v}\rangle$ and the local maximum between $50 < x < 200$ m of V_{TGE}, denoted by $\langle\overline{v}\rangle_m$ and $V_{\mathrm{TGE}m}$, respectively, are presented in Figure 16. The maximum value $V_{\mathrm{TGE}m}$ is located at $x = 123$ m for beach 1 and at $x = 91$

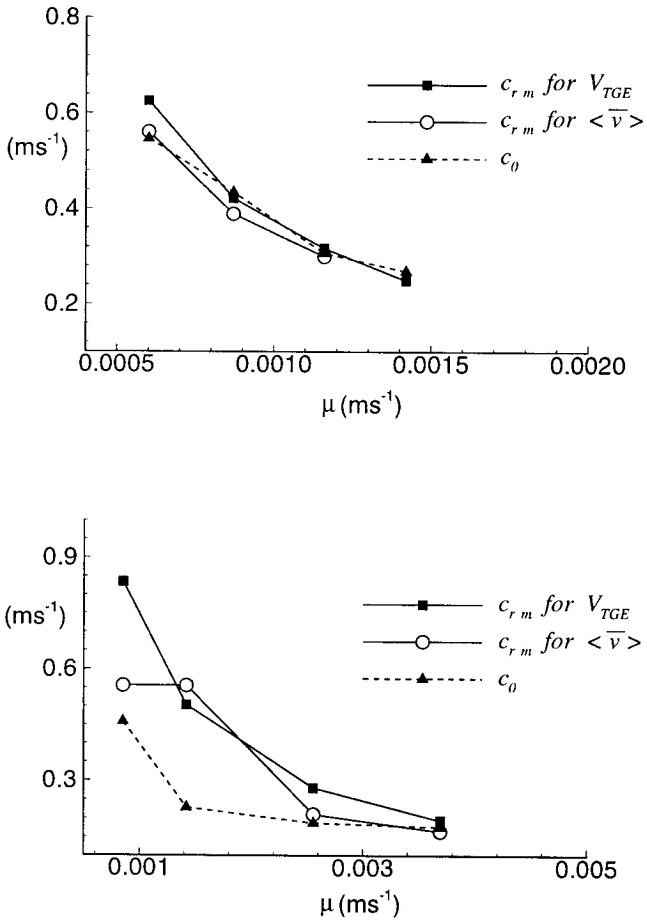

Figure 15. Phase velocities c_{rm} of the most unstable mode from linear stability theory applied to V_{TGE} and $\langle\overline{v}\rangle$ and the observed phase velocities c_0 for experiments on (top) beach 1 and (bottom) beach 2 for different values of μ.

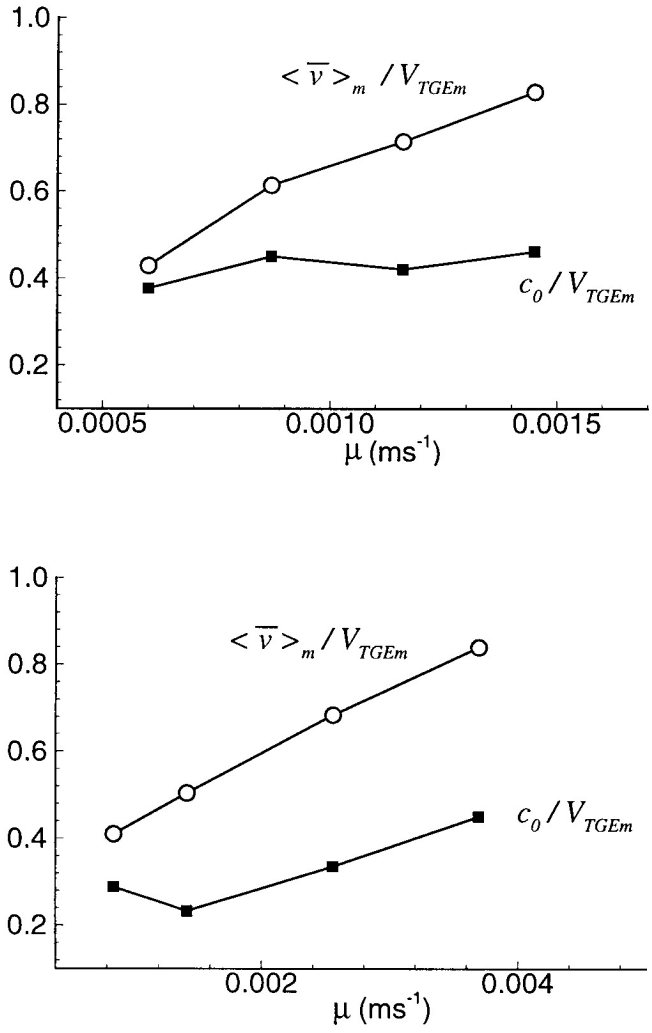

Figure 16. Ratios of velocities involving the observed propagation velocity c_0 and the maximum values, denoted by subscript m, of V_{TGE} and $\langle\overline{v}\rangle$ from experiments on (top) beach 1 and (bottom) beach 2 as a function of μ.

m for beach 2. Also plotted is the ratio of the observed alongshore propagation velocities c_0, determined from wavenumber-frequency spectra, to $V_{\mathrm{TGE}m}$. Values of $c_0/V_{\mathrm{TGE}m}$ generally decrease with decreasing friction. This effect is somewhat more pronounced for beach 2 (Figure 16, bottom) than for beach 1 (Figure 16, top). Both beaches show nearly linear decreases of $\langle\overline{v}\rangle_m/V_{\mathrm{TGE}m}$ with decreasing μ from ~0.8 for beach 1 and 0.9 for beach 2 at high values of μ to ~0.4 at low friction for both beaches. This result is consistent with the variation in across-shore structure of $\langle v\rangle$ relative to V_{TGE} as μ decreases (Figures 10 and 11).

To assess effects of different forcing profiles, additional nonlinear experiments were run with forcing specified by the observed mean velocity profiles $\langle\overline{v(x)}\rangle$ from experiments on beach 1 at the same values of μ, i.e., $V = \langle\overline{v(x)}\rangle\left[1 + \epsilon b(y)\right]$. For $\mu = 0.00145$ m s^{-1} the flow forced with $\langle\overline{v(x)}\rangle$ is linearly stable. Time series of the across-shore velocity for $\mu = 0.00087$ and 0.00060 m s^{-1} are shown in Figure 17. For $\mu = 0.00087$ m s^{-1} the flow develops into an equilibrated shear wave with alongshore wavelength of 256 m, in as close agreement with the linear theory as possible in the 1280 m domain. For $\mu = 0.00060$ m s^{-1} the flow forced by $\langle\overline{v}\rangle$ develops into fluctuating shear waves similar to the response observed for $\mu = 0.00116$ m s^{-1} with V_{TG} forcing as shown in Figure 4. For $\mu = 0.00060$ m s^{-1} the dominant alongshore wavelength, obtained from the alongshore wavenumber-frequency spectra of $u(x_0, y, t)$ at $x_0 = 100$ m, is 240 m. The alongshore propagation velocities are $c_0 = 0.411$ and 0.585 m s^{-1} for $\mu = 0.00087$ and 0.00060 m s^{-1}, respectively, very similar to the results from linear theory and the V_{TG}-forced experiments. The results of these experiments forced with $\langle\overline{v}\rangle$ point to the difficulty of predicting the shear wave climate based on the measured mean velocity profiles. The lower velocity maxima and weaker shear in the $\langle\overline{v}\rangle$ profiles compared to the V_{TGE} profiles result in less turbulent flow response for the same values of μ.

4. Summary

Results of numerical experiments of the nonlinear development of alongshore currents over two barred beaches have been presented. In these experiments the forcing is coupled to the bottom topography by the *Thornton and Guza* [1986] model, which parameterizes the effects of obliquely incident breaking surface waves and translates that into alongshore momentum input. The flow response depends on the dimensionless parameter Q. Different parameter ranges of Q are explored (Table 1) by varying the bottom friction coefficient μ for a fixed barred beach topography. Numerical experiments have been conducted here across a range of bottom friction coefficients $\mu < \mu_C$ that produce significantly different flow regimes. The qualitative features of the results appear to be robust and independent of the particular beach topography. The flows are started

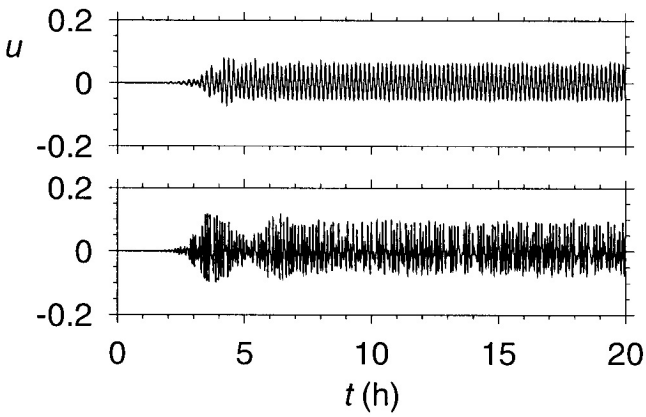

Figure 17. Time series of across-shore velocity component $u(x_0, y_0, t)$ at $x_0 = 125$ m, $y_0 = 0$ from experiments on beach 1 forced with $\langle\overline{v}\rangle$ profiles with (top) $\mu = 0.00087$ and (bottom) 0.00060 m s^{-1}.

from rest. During the initial transient period, propagating disturbances grow with wavelengths and phase speeds that are well predicted by linear stability theory. There are roughly four classes of nonlinear flows that develop after the unstable perturbations grow in amplitude. For relatively large μ ($< \mu_C$), equilibrated shear waves develop that stabilize at finite amplitude and propagate alongshore at a uniform phase velocity. The wavelength and phase speeds of the equilibrated waves are in agreement with the predictions for the fastest-growing linearly unstable mode. The second class of flows that develop, at slightly lower friction, are fluctuating vorticity waves. The vorticity fields associated with theses waves generally maintain the structure of individual positive vortices, but these fluctuate in an irregular fashion within the confines of the mean alongshore current as they propagate alongshore at a nearly constant phase speed. Occasionally, these positive vortices will merge as one vortex overtakes another. The third class of flows is characterized by the shedding of vortex pairs of opposite sign that break away from the nearshore region and propagate offshore of the sandbar. The final class of flows, at still lower values of bottom friction, fits the description of a turbulent shear flow. Here the alongshore currents are dominated by energetic eddies that continuously form, merge, and interact in a complex fashion. In these flows, oppositely signed vortex pairs and single vortices are continuously shed from the region of alongshore current, creating an offshore eddy field with significant turbulent kinetic energy measured out to distances 500–700 m offshore.

Wavenumber-frequency spectra show that for the equilibrated shear waves the energy is tightly confined around the particular ω and k values corresponding to the dominant frequency and wavenumber of the steadily propagating regular waves. As the friction is decreased, the energy spreads progressively to higher wavenumbers and frequencies generally along a line corresponding to the phase velocity of the vorticity waves $\omega/k = c_0$. It is worth noting the strong qualitative differences in appearances of the spectra for the equilibrated shear waves compared to the more irregular flows at low friction.

The T-G model has evidently been successful at making mean alongshore current predictions on plane (i.e., constant slope) beaches [e.g., *Thornton and Guza*, 1986]. T-G model predictions over barred beaches, however, have not been successful when compared with field observations [*Church and Thornton*, 1993]. When a sandbar is present, the T-G model predicts the largest alongshore currents over the sandbar and near the shore with relatively weaker currents in the trough. This leads to two distinct regions of momentum input (jets). Typically, however, the observed alongshore current is found to be just as strong in the trough as it is over the bar or near the shore [*Smith et al.*, 1993]. The time mean alongshore currents $\langle v \rangle$ plotted in Figures 10 and 11 demonstrate that turbulent eddies caused by shear instabilities of the alongshore current may be responsible for diffusing alongshore momentum into the trough. The horizontal diffusion of mean alongshore momentum is supported by the gradient of the Reynolds stress $\langle \overline{(huv)_x} \rangle$. Thus across-shore diffusion of the mean alongshore momentum by larger-scale current instabilities may be an important consideration in reconciling field observations with predictions from T-G type models.

In each of the four classes of shear flows that develop, flow features propagate alongshore at a dominant characteristic velocity. These propagation velocities are clearly revealed by the energy spectra in wavenumber-frequency space and by time- and space-lagged correlations. By utilizing a coordinate system translating alongshore at the observed characteristic velocity, useful information about the magnitude and structure of the mean and fluctuating parts of the vorticity fields can be obtained. In this way it is shown quantitatively that for the equilibrated waves, nearly all of the vorticity is contained in the mean field. It is also clearly shown how the magnitudes of the fluctuations increase as μ decreases.

Application of linear stability analysis to the time-averaged alongshore currents $\langle \overline{v} \rangle$ (Figure 14) is motivated by similar applications to field data [e.g., *Dodd et al.*, 1992]. In those studies, linear stability analysis of observed time-averaged alongshore velocity profiles have been used to estimate wavelengths and phase speeds of shear instabilities. These estimates appear to agree with the observed values. The generally good agreement could lead to the interpretation of observed shear instabilities as being weakly nonlinearly equilibrated shear waves. We have shown here (Figures 14–16) that linear stability analysis of time-averaged velocity profiles from flows with equilibrated shear waves can imply stability and that linear stability analysis from flows with irregular fluctuations can give predictions of unstable waves with propagation velocities and alongshore wavelengths in reasonable agreement with the observed values. In general, the growth rates of the unstable waves are substantially smaller than those found with the V_{TGE} profiles. Forcing with the mean $\langle \overline{v} \rangle$ profiles from the V_{TG} experiments leads to nonlinear flows with weaker shear wave environments. The $\langle \overline{v} \rangle$ experiments, however, produce similar alongshore wavelengths, propagation velocities, and time mean alongshore velocity profiles compared to their more turbulent counterparts forced with V_{TG}. The implication is that good agreement of measured values of propagation velocities and wavelengths with predicted values obtained from linear stability analyses of time-averaged velocity profiles does not necessarily imply a weakly nonlinear flow regime. It is possible that energetic eddy fields, which have yet to be clearly identified from existing analyses of field observations, may be present in the nearshore region.

Several of the findings in this study of shear waves over barred beaches with forcing from the *Thornton and*

Guza [1986] model differ from the results found by *Allen et al.* [1996] for shear wave behavior over plane beaches. One of the most significant differences is that over barred beaches, lowering the friction spreads significant energy in the alongshore wavenumber-frequency spectra to smaller length and shorter timescales. On plane beaches at low friction, shorter-wavelength disturbances tend to merge, creating propagating disturbances with longer characteristic length scales and longer timescales. Possible causes for the different flow development include the different velocity profiles predicted by the T-G model. The T-G model applied to plane beaches forces a single broad alongshore jet, qualitatively similar to the idealized forcing profiles assumed in *Allen et al.* [1996], while applications to barred beaches produce narrower twin jets. Another reason for the difference might be the dynamical effect of the bottom topography of the sandbar on the instabilities that develop in the alongshore currents. These aspects of the problem are under investigation. Preliminary results indicate that both effects acting together, as in the present experiments, are necessary to produce the barred beach behavior found here.

Appendix A: Beach Bathymetry

The bathymetry profiles $h(x)$ for beaches 1 and 2 are presented here. The depth profile in Figure 2 (top) is described by

$$h(x) = b\,x + A_1 \exp\left[-\left(\frac{x-x_1}{L_1}\right)^2\right] + A_2 \exp\left[-\left(\frac{x-x_2}{L_2}\right)^2\right], \quad \text{(A1)}$$

where $b = 0.0125$ is the linear beach slope, $x_1 = 40$ m is the location of a nearshore trough with amplitude $A_1 = 0.9$ m and characteristic width $L_1 = 20$ m, and $x_2 = 180$ m is the center of an offshore trough with amplitude $A_2 = 0.7$ m and width $L_2 = 50$ m. This profile is generated to approximate bathymetry from the Superduck field experiment on October 15, 1986, at Duck, North Carolina, in which a shore-parallel sandbar was located at ~80 m offshore [e.g., *Dodd et al.*, 1992]. This beach profile is referred to as beach 1.

The depth profile in Figure 2 (bottom) from *Lippmann et al.* [1998], is

$$h(x) = A_1 \tanh\left(\frac{b_1\,x}{A_1}\right) + \frac{A_1}{\gamma}\left[\frac{b_1\,x}{A_1} - \tanh\left(\frac{b_1\,x}{A_1}\right)\right] - A_2 \exp\left[-5\left(\frac{x-x_C}{x_C}\right)^2\right], \quad \text{(A2)}$$

where $b_1 = \tan\beta_1 = \tan(0.075)$ is the linear beach slope close to the shore, $b_2 = \tan\beta_2 = \tan(0.0064)$ is the beach slope offshore of the sandbar, $\gamma = b_1/b_2$, $x_C = 80$ m is the location of the sandbar, and the coefficients $A_1 = 2.97$ and $A_2 = 1.5$. This beach profile is an approximate fit to topography measured at Duck, North Carolina, October 11, 1990, as part of the DELILAH (Duck Experiment on Low-frequency and Incident-band Longshore and Across-shore Hydrodynamics) field experiment and is referred to as beach 2.

Appendix B: Thornton and Guza Model

The alongshore momentum equation is forced using results from the *Thornton and Guza* [1986] model with a constant linear bottom friction coefficient [see also [*Thornton and Guza*, 1983]. The T-G model, specialized to the case of a constant linear bottom friction coefficient μ, predicts an alongshore velocity profile given by *Thornton and Guza* [1986, equation (17)]

$$V_{\mathrm{TG}}(x) = \frac{1}{\rho_0 \mu}\frac{\sin\,\hat{\alpha}_0}{C_0}\langle\epsilon_b\rangle\ , \quad \text{(B1)}$$

where $C_0 = gT_p/2\pi$ is the deep water surface gravity wave phase speed, T_p is the wave period of the peak of the wave energy spectrum (assumed to be narrowband), $\hat{\alpha}_0$ is the mean offshore wave angle (measured from the onshore direction), ρ_0 is the fluid density (1000 kg m^{-3}), and μ is a specified constant value for the bottom friction coefficient. The dissipation function $\langle\epsilon_b(x)\rangle$ is determined using [*Thornton and Guza*, 1983, equation (26)]

$$\langle\epsilon_b(x)\rangle = \frac{3\sqrt{\pi}\rho_0 g B^3 f_p}{16}\frac{H_{\mathrm{rms}}^5(x)}{\gamma^2 h^3(x)} \times\left\{1-\left[1+\left(\frac{H_{\mathrm{rms}}(x)}{\gamma h(x)}\right)^2\right]^{-5/2}\right\}. \quad \text{(B2)}$$

Here $h(x)$ is the water depth; $H_{\mathrm{rms}}(x)$ is the rms wave height distribution for a narrow-banded wave field; $f_p = 1/T_p$ is the peak wave frequency; γ is the breaker index, taken here to be 0.43 (following typical values utilized by *Thornton and Guza* [1986]); g is the gravitational acceleration (9.8 m s^{-2}); and B is an empirical constant that accounts for various breaker intensities. Optimal values of B in the T-G model have been reported in the range between $B = 1.5$ [*Thornton and Guza*, 1983] and $B = 0.8$ [*Thornton and Guza*, 1986]. Here we take $B = 1.2$.

The rms wave height H_{rms} is determined by integrating the relation [*Thornton and Guza*, 1986, equation (3)]

$$\frac{d(E\,C_g\cos\hat{\alpha})}{dx} = \langle\epsilon_b\rangle \quad \text{(B3)}$$

from an offshore location to the beach. Equation (B3) indicates that the across-shore gradient of the wave field energy flux $E\,C_g\cos\hat{\alpha}$, where $E = \rho g H_{\mathrm{rms}}^2/8$, is balanced by the dissipation of wave energy from breaking. The term $C_g(x)\,\cos[\hat{\alpha}(x)]$ represents the onshore component of the group velocity vector of the oncoming wave field. The derivative on the left-hand side of (B3),

$$\frac{d(\frac{1}{8}\rho g H_{\rm rms}^2 C_g \cos\hat{\alpha})}{dx} = \langle \epsilon_b \rangle \ , \qquad \text{(B4)}$$

is discretized using one-sided finite differences. The difference equation is solved with a marching procedure in the onshore direction from an offshore location at $x = x_I$, outside of the region of wave breaking, to the shore. Conditions required at $x = x_I$ include $H_{\rm rms}(x_I)$ and T_P, and $\hat{\alpha}(x_I)$ is determined from the specified deep water wave angle $\hat{\alpha}_0$ using Snell's law.

The x component of the group velocity C_{gx} varies with depth in shallow water and is determined from [*Thornton and Guza*, 1983, equation (10)]

$$C_{gx}(x) = C(x)\, n(x) \cos\left[\hat{\alpha}(x)\right] \ , \qquad \text{(B5)}$$

where $C(x)$ is the wave phase velocity,

$$n(x) = \frac{1}{2}\left[1 + \frac{2kh}{\sinh(2kh)}\right] \ , \qquad \text{(B6)}$$

and where $\hat{\alpha}(x)$ is determined through Snell's law by

$$\hat{\alpha}(x) = \sin^{-1}\left[\frac{C(x)\sin\ \hat{\alpha}_0}{C_0}\right] \ . \qquad \text{(B7)}$$

The phase velocity $C(x) = \sigma/k(x)$ is found by utilizing the dispersion relation $\sigma^2 = gk\tanh(kh)$ with $\sigma = 2\pi/T_P$ to find $k(x)$. We have used an approximate method, based on that of Eckart [see, e.g., *Dean and Dalrymple*, 1991, section 3.5], to obtain $k(x)$. This approximate method produces results for both $k(x)$ and $V_{\rm TG}(x)$ that are equivalent within a few percent to exact solutions obtained using iteration of the dispersion relation. The Eckart approximation is implemented using $C(x) = 2\pi/\left[T_p k(x)\right]$ with $\sigma^2 = (2\pi/T_p)^2$,

$$k'(x) = (\sigma^2/g)\left[\tanh(\sigma^2 h/g)\right]^{-1/2} \ , \qquad \text{(B8a)}$$

$$k''(x) = \sigma^2/\left[g\tanh(k'h)\right] \ , \qquad \text{(B8b)}$$

$$k(x) = \frac{1}{2}\left[k'(x) + k''(x)\right] \ . \qquad \text{(B8c)}$$

For beach 1 and beach 2, $V_{\rm TG}(x)$ (B1) was calculated assuming $T_P = 8$ s, $H_{\rm rms}(x_I) = 0.7$ m, and $\hat{\alpha}_0 = 20°$, where $x_I = 1000$ m. For beach 1, $h(x_I) = 12.5$ m, and for beach 2, $h(x_I) = 9.2$ m.

Appendix C: Linear Stability

It is most convenient to start an investigation of the linear stability of the alongshore current $v = V_{\rm TGE}(x)$ by considering the equation for potential vorticity $q = \zeta/h$, which may be derived from (2.1):

$$q_t + uq_x + vq_y - (\mu/h)(V/h)_x + (\mu/h)\left[(v/h)_x - (u/h)_y\right] + (\nu/h)\nabla^4\zeta = 0 \, . \qquad \text{(C1)}$$

We write the variables as

$$u = \tilde{u}, \quad v = V_{\rm TGE} + \tilde{v} \, , \qquad \text{(C2a)}$$

$$h\tilde{u} = -\tilde{\psi}_y, \quad h\tilde{v} = \tilde{\psi}_x \, , \qquad \text{(C2b)}$$

$$\tilde{\zeta} = \tilde{v}_x - \tilde{u}_y, \quad \tilde{q} = \tilde{\zeta}/h \, , \qquad \text{(C2c)}$$

$$\tilde{\zeta}_{\rm TGE} = V_{{\rm TGE}x}, \quad q_{\rm TGE} = \zeta_{\rm TGE}/h \, , \qquad \text{(C2d)}$$

where

$$V = V_{\rm TG}(x) \, , \qquad \text{(C2e)}$$

and where $V_{\rm TGE}(x)$ satisfies (10).

Substituting (C2) in (C1) and retaining linear terms, we obtain

$$\tilde{q}_t + V_{\rm TGE}\tilde{q}_y + \tilde{u}q_{{\rm TGE}x} + (\mu/h)\left[(\tilde{v}/h)_x - (\tilde{u}/h)_y\right] + (\nu/h)\nabla^4\tilde{\zeta} = 0 \, , \qquad \text{(C3)}$$

which provides a single equation for the perturbation streamfunction $\tilde{\psi}$. We consider solutions of the form

$$\tilde{\psi} = Re\Big\{\phi(x)\exp\left[ik(y - ct)\right]\Big\}, \qquad \text{(C4)}$$

where ϕ and c may be complex ($c = c_r + ic_i$) and where Re denotes the real part. The resulting equation for ϕ is

$$\left(V_{\rm TGE} - c - \frac{i\mu}{kh}\right)(\phi_{xx} - \frac{h_x}{h}\phi_x - k^2\phi) - h\left(\frac{V_{{\rm TGE}x}}{h}\right)_x \phi + \frac{i\mu h_x}{kh^2}\phi_x - \frac{i\nu h}{k}(\hat{\zeta}_{xxxx} - 2k^2\hat{\zeta}_{xx} + k^4\hat{\zeta}) = 0 \, , \qquad \text{(C5a)}$$

where

$$\hat{\zeta} = (\phi_{xx} - (h_x/h)\phi_x - k^2\phi)/h \, . \qquad \text{(C5b)}$$

The boundary conditions for (C5a) follow from (6) and (7)

$$\phi = 0 \qquad x = 0, L^{(x)} \, , \qquad \text{(C6a)}$$

$$\hat{\zeta} = \hat{\zeta}_{xx} = 0 \qquad x = 0, L^{(x)} \, . \qquad \text{(C6b)}$$

Following the procedure in *Allen et al.* [1996], finite difference methods are utilized to solve the linear stability problem (C5) and (C6). A centered, second-order difference scheme that is consistent with the difference approximations used for the shallow-water equations is employed. The resulting difference approximations for (C5) are the same as those described in *Allen et al.* [1996] with the exception that here the biharmonic diffusion terms are included and boundary conditions (C6b) are added.

This procedure results in a set of algebraic equations.

$$\mathbf{A}\boldsymbol{\phi} = c\mathbf{B}\boldsymbol{\phi} \, , \qquad \text{(C7)}$$

where $\mathbf{A}$ and $\mathbf{B}$ are matrices and $\boldsymbol{\phi}$ is a vector. From (C7) we obtain

$$\mathbf{B}^{-1}\mathbf{A}\boldsymbol{\phi} = c\boldsymbol{\phi} \, , \qquad \text{(C8)}$$

which may be readily solved for eigenvalues c and eigenvectors $\boldsymbol{\phi}$.

The grid resolution utilized is the same as in the corresponding numerical experiments.

Appendix D: Observed Growth Rates

Linear growth rates from the stability analysis (Figure 3) are compared to the observed rates of growth in the nonlinear simulations. A measure of the kinetic energy in different alongshore Fourier modes is calculated at $x_0 = 125$ m by utilizing Fourier transforms of $u(x_0, y, t)$ and $v(x_0, y, t)$ in the alongshore direction.

Assuming Fourier component wave solutions for the variables u and v of the form $u(y) = \hat{u}(k)e^{iky}$ and periodicity in y with period $L^{(y)}$, the fields can be expanded in truncated Fourier series with corresponding Fourier coefficients

$$\hat{u}(k_n) = \frac{1}{N}\sum_{j=0}^{N-1} u(y_j)e^{-ik_n y_j}, \qquad \text{(D1)}$$

where $y_j = L^{(y)}j/N$, $j = 0, 1, \cdots, N-1$; and k_n are the wave numbers $2\pi n/L^{(y)}$. The mode numbers n range from $n = 0, 1, \cdots, N-1$, where N is the total number of grid points in y [*Canuto et al.*, 1988]. The kinetic energy is defined as a function of the alongshore wavenumbers with

$$\mathrm{KE}(k,t) = \frac{1}{2}\left[\hat{u}(k_n,t)\hat{u}^*(k_n,t) + \hat{v}(k_n,t)\hat{v}^*(k_n,t)\right], \qquad \text{(D2)}$$

where $\hat{u}^*$ is the complex conjugate of $\hat{u}$.

Experiments were conducted with infinitesimal ($\epsilon = 10^{-10}$) forced perturbations added to the mean profiles (8) and (9) with $J = 12$ and random phase shifts. Mode 0, the mean alongshore current, was started at the steady state frictionally balanced amplitude with $v_0 = V_{\mathrm{TGE}}(x)$, $u_0 = 0$. This differs from the method used in the other experiments, where the flows were started from rest. In this experiment the flow was started from the frictionally balanced steady state value so that the linear growth rates would not vary over the start-up period as the strength of the mean current increased.

The linear growth rates are confirmed in the nonlinear model. The energy in each alongshore Fourier mode was calculated as a function of time, and the growth rate of energy was compared to the predictions from the linear analysis. Results are shown for beach 1 in Figure 18 for the case with $\mu = 0.00087$ m s^{-1} where the energy for mode numbers 1–19 is plotted on a log scale as a function of time. The nearly linear slope of the energy for times between 40 and 120 min for modes 4 and 5 and for times between 60 and 100 min for mode 6 were used to estimate the growth rates of the fastest-growing modes in the simulations. As predicted by linear theory, mode 5 (256 m) has the fastest growth rate. Ratios of the observed growth rates in the nonlinear experiments to the predicted rates from linear theory for the three fastest-growing modes, mode 4 (320 m), mode 5 (256 m), and mode 6 (213 m) are 0.9921, 0.9913, and 0.9912, respectively. This is very close agreement between the nonlinear model results and the linear predictions. In each case the observed growth rates are within 1% of the predicted values. Also apparent in Figure 18 is the rapid growth rates of modes 9–19, beginning at approximately $t = 90$–120 min. These modes are linearly stable but are evidently influenced by a different type of instability mechanism when the primary modes begin to grow to appreciable amplitude. The growth rates for

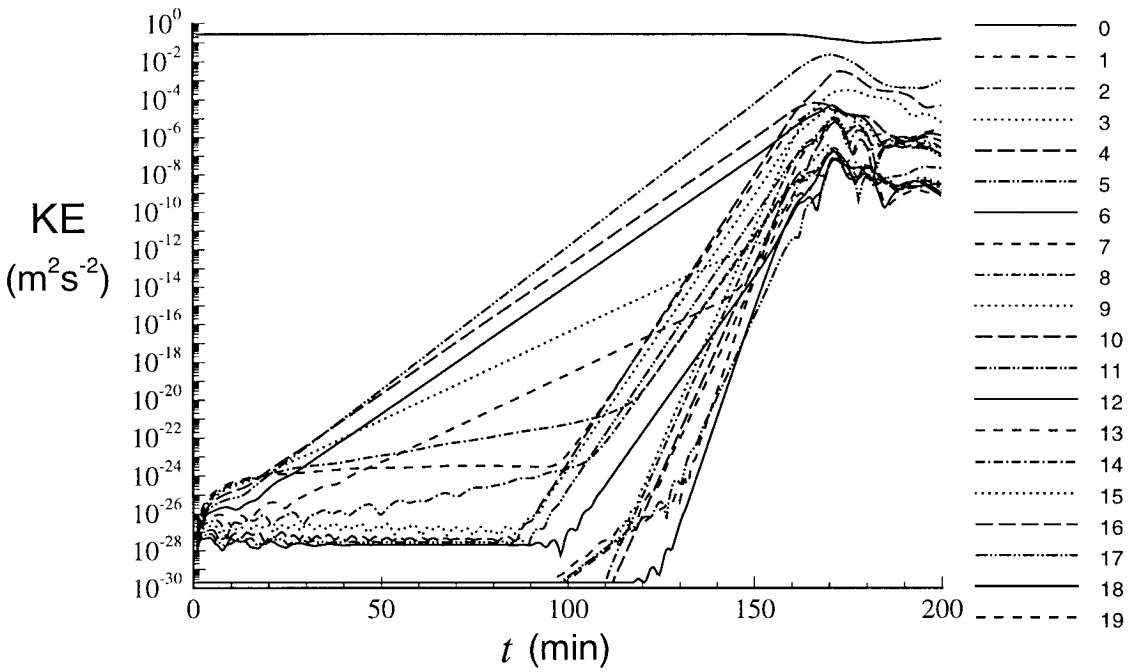

Figure 18. Kinetic energy KE (D2) in different alongshore wavenumbers corresponding to Fourier mode numbers $n = 0, 19$ as a function of time at $x_0 = 125$ m.

these modes are even larger than the growth rates of the fastest-growing linearly unstable modes. We note that these modes only begin to grow after the energy in the initially fastest growing modes has increased several orders of magnitude from the initial levels.

Acknowledgments. This research was supported by the Office of Naval Research (ONR) Coastal Dynamics Program under grant N00014-95-1-0047. Support was also provided for J.S.A. and P.A.N. by ONR grant N00014-93-1-1301, for J.S.A. by NSF grant OCE-9314317, and for R.A.H. by ONR grant N00014-96-1-0237. Supercomputer support was provided by the College of Oceanic and Atmospheric Sciences, OSU, through a grant to M. R. Abbott from the NASA Earth Observing System program.

References

Allen, J. S., P. A. Newberger, and R. A. Holman, Nonlinear shear instabilities of alongshore currents on plane beaches, *J. Fluid Mech., 310,* 181–213, 1996.

Battjes, J., Modeling of turbulence in the surf zone, paper presented at the Symposium on Modeling Techniques, pp. 1050–1061, Am. Soc. of Civ. Eng., San Francisco, Calif., 1975.

Bowen, A. J., and R. A. Holman, Shear instabilities of the mean longshore current, 1, Theory, *J. Geophys. Res., 94,* 18,023–18,030, 1989.

Canuto, C., M. Y. Hussaini, A. Quarteroni, and T. A. Zang, *Spectral Methods in Fluid Dynamics,* 557 pp., Springer-Verlag, New York, 1988.

Church, J. C., and E. B. Thornton, Effects of breaking wave induced turbulence within a longshore current model, *Coastal Eng., 20,* 1–28, 1993.

Dean, R. G., and R. A. Dalrymple, *Water Wave Mechanics for Engineers and Scientists,* 353 pp., World Sci., River Edge, New Jersey, 1991.

Deigaard, R., E. D. Christensen, J. S. Damgaard, and J. Fredsoe, Numerical simulation of finite amplitude shear waves and sediment transport, in *Coastal Engineering 1994: Proceedings of the Twenty-Fourth International Conference,* vol. 2, edited by B. L. Edge, pp. 1919–1933, Am. Soc. of Civ. Eng., Reston, VA, 1995.

Dodd, N., On the destabilization of a longshore current on a plane beach: Bottom shear stress, critical conditions, and onset of instability, *J. Geophys. Res., 99,* 811–828, 1994.

Dodd, N., and E. B. Thornton, Longshore current instabilities: Growth to finite amplitude, in *Coastal Engineering 1992: Proceedings of the Twenty-Third International Conference,* vol. 3, edited by B. L. Edge, pp. 2655–2668, Am. Soc. of Civ. Eng., Reston, Va, 1993.

Dodd, N., J. Oltman-Shay, and E. B. Thornton, Shear instabilities in the longshore current: A comparison of observation and theory, *J. Phys. Oceanogr., 22,* 62–82, 1992.

Drazin, P. G., and W. H. Reid, *Hydrodynamic Stability,* Cambridge Univ. Press, New York, 1981.

Elgar, S., T. H. C. Herbers, and R. T. Guza, Reflection of ocean surface gravity waves from a natural beach, *J. Phys. Oceanogr., 24,* 1503–1511, 1994.

Falques, A., V. Iranzo, and M. Caballeria, Shear instability of longshore currents: Effects of dissipation and nonlinearity, in *Coastal Engineering 1994: Proceedings of the Twenty-Fourth International Conference,* vol. 2, edited by B. L. Edge, pp. 1983–1997, Am. Soc. of Civ. Eng., Reston, Va, 1995.

Lippmann, T. C., T. H. C. Herbers, and E. B. Thornton, Gravity and shear wave contributions to nearshore infragravity motions, *J. Phys. Oceanogr.*, in press, 1998.

Oltman-Shay, J., P. A. Howd, and W. A. Birkemeier, Shear instabilities of the mean longshore current, 2, Field data, *J. Geophys Res., 94,* 18,031–18,042, 1989.

Ozkan-Haller, H. T., and J. T. Kirby, Numerical study of low frequency surf zone motions, in *Coastal Eng. 1996: Proceedings of the Twenty-Fifth International Conference on Coastal Engineering,* vol. 2, edited by B. L. Edge, pp. 1361–1374, Am. Soc. of Civ. Eng., Reston, Va, 1997.

Smith, J. M., M. Larson, and N. C. Kraus, Longshore current on a barred beach: Field measurements and calculation, *J. Geophys Res., 98,* 22,717–22,731, 1993.

Svendsen, I. A., Wave heights and set-up in a surf zone, *Coastal Eng., 8,* 347–364, 1984.

Thornton, E. B., and R. T. Guza, Transformation of wave height distribution, *J. Geophys Res., 88,* 5925–5938, 1983.

Thornton, E. B., and R. T. Guza, Surf zone longshore currents and random waves: Field data and models, *J. Phys. Oceanogr., 16,* 1165–1178, 1986.

J. S. Allen, R. A. Holman, P. A. Newberger, and D. N. Slinn, College of Oceanic & Atmospheric Sciences, Oregon State University, 104 Ocean Admin Bldg., Corvallis, OR 97331. (email: jallen@oce.orst.edu; holman@oce.orst.edu; newberg@oce.orst.edu; slinn@oce.orst.edu;)

(Received March 25, 1997; revised November 17, 1997; accepted February 12, 1998.)